Summer 2024

Directed Energy Deposition Processing-Performance Relationship of Af9628

Mianqing Yang

Missouri University of Science and Technology

Recommended Citation

Yang, Mianqing, "Directed Energy Deposition Processing-Performance Relationship of Af9628" (2024). *Masters Theses*. 8191.
https://scholarsmine.mst.edu/masters_theses/8191

DIRECTED ENERGY DEPOSITION PROCESSING-PERFORMANCE RELATIONSHIP OF AF9628

by

MIANQING YANG

A THESIS

Presented to the Graduate Faculty of the

MISSOURI UNIVERSITY OF SCIENCE AND TECHNOLOGY

In Partial Fulfillment of the Requirements for the Degree

MASTER OF SCIENCE IN MANUFACTURING ENGINEERING

2023

Approved by:

Frank W. Liou, Advisor
Ashok Midha
Serhat Hosder

ABSTRACT

AF9628 low alloy steel is a novel steel known for its low cost, high hardness, and outstanding tensile performance. However, the processing methods of AF9628 have been less studied in the additive manufacturing field. As the balance of hardness and tensile results is closely related to the cooling process during manufacturing process window and its relationship to resultant tensile properties is explored. By using the DED method, specimens of this steel are successfully fabricated, and tensile test results are obtained. The AF9628 steel can be manufactured for tailored properties with the DED process by controlling the cooling method. This work is funded by ARL - GVSC under cooperative agreement W911NF-20-2-0251.

ACKNOWLEDGMENTS

This work is funded by ARL - GVSC under cooperative agreement W911NF-20-2-0251. I sincerely thank my advisor, committee members, lab mates, friends, and family for their support through my master program.

TABLE OF CONTENTS

Page

SECTION

LIST OF ILLUSTRATIONS

LIST OF TABLES

NOMENCLATURE

Symbol	Description
LP	Laser Power
SS	Scan Speed
ED	Energy Density
YS	Yield Stress
UTS	Ultimate Tensile Strength

1. INTRODUCTION

The AF9628 is a type of novel low alloy invented by the American Air Force which is widely used in the military field. Its high tensile preference and low cost enable it to be an outstanding material for producing weapons. The AF9628 low alloy has been studied with selective laser melting (SLM) process. A mean YS (yield strength) of over 1500Mpa, a mean UTS (Ultra tensile strength) of over 1700Mpa, and a mean elongation of over 10% are tensile tested along TD-SD SD-BD and BD-TD directions [1]. However, the AF9628 low alloy steel has been rarely studied in the DED (direct energy deposition) process. It is likely that the tensile performance (YS, UTS, elongation) of the AF9628 alloy steel can be further improved. Once it is improved, the AF9628 low alloy steel can also become an ideal material for 3D rapid repair. This paper meanly includes the study of the tensile results from the AF9628 DED process, which can be referred for the study of AF9628 for 3D rapid repair.

2. EXPERIMENTAL STEUP

2.1. MATERIAL

Steel alloy is the type of alloy being the most widely used in the industry. Through the history of metallurgy, thousands of types of steel have in invented for tailored properties. In this study we focus on the properties of the novel low alloy steel AF9628 manufactured by DED process.

2.1.1. Introduction to AF9628. The AF9628 low alloy is devolved by Dr. Rachel Abrahams. This type of novel alloy interests the industry for its ultra-high-strength and low cost. As the costly element such as Ni is limited contained, the cost of AF9628 is lower than the conventional steel. It is also highly weldable since it does not contain any high melting point elements such as W or Co. On the other hand, all these properties make the AF928 steel a future material for additive manufacturing process, which makes it doable to produce parts of more complex geometry [1].

2.1.2. Powder Image. The AF9628 low alloy powder we used in this study is the commercial AM powder produced by Powder Alloy Corporation. The AF9628 particle size is analyzed by the AFA mode on the ASPEX Machine. The powder images (shown in Figure 2.1) are taken ranging from x120 through x 200. As shown in these images, the AF9628 powders we purchased for this study are not perfectly spherical. [13] [14] Some of the particles are in an elliptical shape.

2.1.3. AF9628 Particle Size Distribution. The particle distribution is shown in Figure 2.2. There are 5028 particles analyzed in size. According to Davg, about 39% of the particles are extremely fine(<10µm) 45% of the particles are fine(10-20µm), 13 % of the particles are 20-60µm, and ~3% of the particles are >60µm. The particle size majorly ranges between 5-20 microns. The max population is found between 5-10 microns.

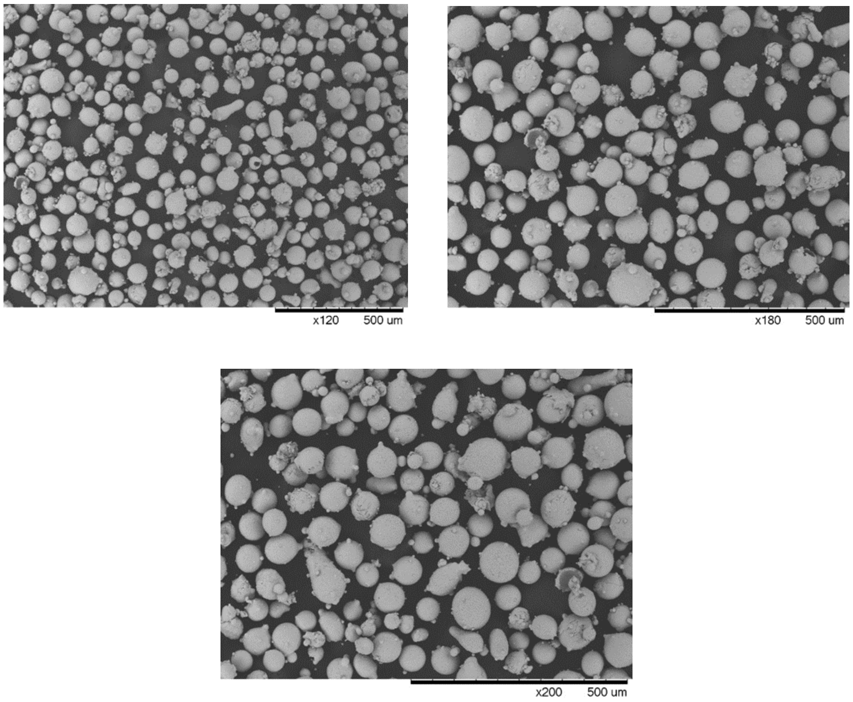

Figure 2.1 AF9628C Powders SEM Image at Magnification of x120 through x200.

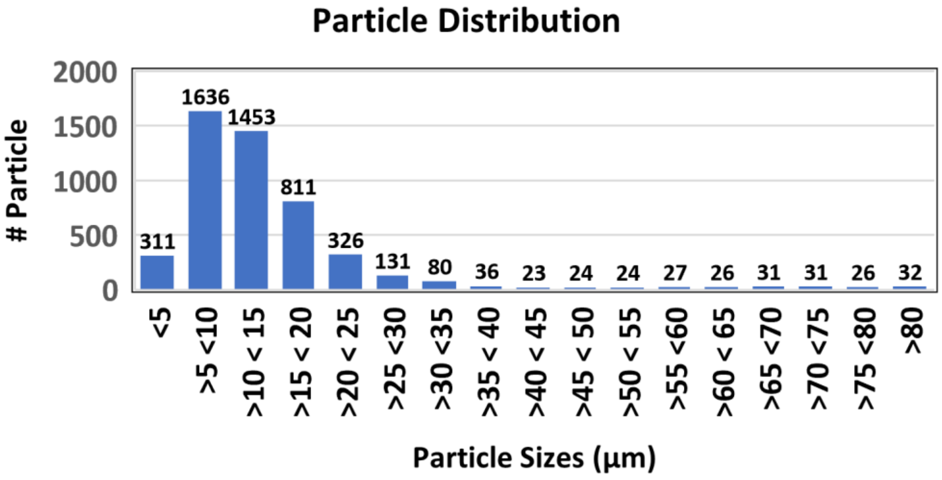

Figure 2.2 AF9628C Particle Distribution.

2.1.4. Chemical Composition AF9628 Powders Used in This Study. The AF9628 low alloy powder we used in this study is the commercial AM powder produced by Powder Alloy Corporation. The Chemical composition comparison between the data given from Carpenter website and from our EDS analysis results are listed below for reference (Table 2.1). The EDS element composite is analyzed from three random spots with the 5.0 kV acceleration voltage, 999 magnifications, and 0.2-micron image pixel size with Hydra scanning electron microscope (SEM). Some of the elements are missing as the EDS has a limited accuracy recognizing the element signals. The lowest reliable element percentage is 1%, only the higher percentage elements can be detected at an acceptable accuracy level. The low percentage elements are unselected at the beginning of the analysis, and those elements listed below 0.5% are included only for reference. The element comparison between the website verses our EDS results are not quite the same. First, as the AF9628C powder used in this study is produced by Powder Alloy Corporation which the exact element composite can be different from the data posted on the carpenter website. Second, our EDS analysis is conducted among only three test spots, the element percentage will keep approaching the real value as the date population increases. Third, as the AF9628C powder is not stainless, it could be oxidized during the shipment and storage periods, and this is the mean reason of a low amount of oxygen is detected in during the EDS analysis. Relatively the difference of EDS results between the virgin powder and the DOE center specimen is smaller which implies that the element composite is stable during the specimen manufacturing process.

The advantage of the AF9628 is obviously its low cost since the content of the expensive elements is low.

Table 2.1 AF9628C Chemical Composition from Carpenter Website vs. Virgin Powder EDS Results vs. DOE Center Specimen EDS Results [2].

	Carpenter website	Virgin Powder Element EDS Analysis		DOE Center Specimen	
Element	weight %	weight %	weight % Error (+/- 2 Sigma)	weight %	weight % Error (+/- 2 Sigma)
C	0.28	0.67	0.02	0.63	0.02
P	0.02	-	-	-	-
Si	1.25	0.96	0.08	0.90	0.08
Ni	3.00	1.88	0.26	2.94	0.26
Mn	1.00	-	-	-	-
S	0.02	-	-	-	-
Cr	2.50	1.65	1.26	1.44	1.25
Mo	1.00	0.32	0.22	0.48	0.22
Fe	Balance	94.15	0.81	93.25	0.80
Ca	0.03	-	-	-	-
Al	0.15	-	-	-	-
N	0.15	-	-	-	-
Zr	0.20	-	-	-	-
O	-	0.37	0.13	0.36	0.13

2.1.5. AF9628 Powders Density Test. The Powder density tester used in this study is “Ultrapyc 1200e” shown in Figure 2.3. First using container which comes with the tester to weigh a randomized amount of powder and load it into the tester. The process starts with pressing the powder with pressure controlled noble gas, then volume can be measured by the tester for three repetitions. Referring to each of the measured volume values three density results are calculated. Finally, by taking the average of the three calculated density values, the gas pore density can be calculated. During the powder density test, 21.257 gm, 12.663 gm, 17.668 gm of AF9628C powder is weighed for randomization. Nitrogen gas is used to compress the powder at 10 psi. Pulse for 3 mins time delay and the run of 3 repetitions are selected in this study. Eventually, the theoretical powder density of 7.818 g/cc is tested at the $Gas\ pore\ density$ of 0.475 ±0.119 (%).


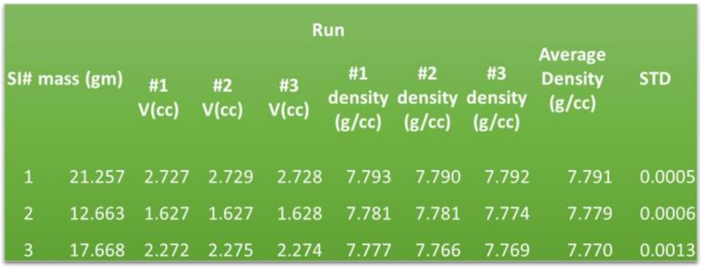

Sl#	mass (gm)	Run #1 V(cc)	#2 V(cc)	#3 V(cc)	#1 density (g/cc)	#2 density (g/cc)	#3 density (g/cc)	Average Density (g/cc)	STD
1	21.257	2.727	2.729	2.728	7.793	7.790	7.792	7.791	0.0005
2	12.663	1.627	1.627	1.628	7.781	7.781	7.774	7.779	0.0006
3	17.668	2.272	2.275	2.274	7.777	7.766	7.769	7.770	0.0013

Figure 2.3 Ultrapyc 1200e. Experimental Settings: Nitrogen Gas, Pressure: 10 PSI, Pulse: 3, Run: 3 Randomization Applied: 21.257 gm, 12.663 gm, 17.668 gm. $Gas\ pore$ D$ensity$: 0.475 ±0.119 (%). Theatrically Powder Density: 7.818 g/cc.

2.2. EXPERIMENT PROCEDURE AND DESIGN

In total, 32 single track deposition samples are being manufactured can cut for micro-tensile test through stage 1 and stage 2. In stage 2, a DOE of 21 samples is conducted for fit models, the critical sample pieces are selected for EBSD analysis.

2.2.1. Stage 2 Powder Sieving. As we are using the purchased AF9628 powder during this study, the property of the powder is manufactured for SLM process, the grain size concentration is in between 10 to 20 microns. A 45 to 150 micron range of powders' grain size is better for the DED process [20]. To improve the sample quality, the powders used in stage 2 have been sieved. The range between 75 to 106 microns is selected for this stage.

2.2.2. Stage 1 & 2 DED Systems. The machine we used to manufacturing sample in stage 1 is named by "Hybrid Cell" (shown in Figure 2.4). It meanly equips a maximum 1000 W pause laser driving a 2 mm diameter laser beam, a wheeling feeder connects to a water-cooled process head with shielding gas nozzle, and a three degree of freedom gentry controlled by the LinuxCNC. The turkey bag is equipped to trap the argon to make sure the air in the process environment is purge out to avoid samples being oxidized.

Figure 2.4 The Hybrid Cell DED system used in Stage 1 Equipped with One 1000w Pause Laser Driving a 2 mm Diameter Laser Beam, One Wheeling Feeder, and One 3-degree of Freedom Gantry Controlled by the LinuxCNC.

The NSF cell shown below in Figure 2.5 is used in stage 2. It is a later built machine in our lab found by National Science Foundation. It is a more powerful machine equipped with one 2000 W diode laser driving a 2 mm diameter laser beam for deposition and one 100 W pulse laser for surface fine finish. As well as six powder feeders, each for one specific type of powder composite to avoid contamination and for specific manufacturing process purposes. Each feeder connects to one individual process head with water-cooled shielding nozzle to prevent clogging from the overheat caused by laser reflection during the process. Instead of using the conventional CNC gantry, the NSF switched to the Nachi robot with six degrees of freedom to manufacture more complicated sample geometries. The process environment is inchambered in a glove box filled up with argon to protect samples being oxidized during the manufacturing process.

Figure 2.5 The NSF Cell Used in Stage 2 Equipped with One 2000 W Diode Laser Driving a 2 mm Diameter Laser Beam and One 100 W Pulse Laser, As Well As Six Powder Feeders, Each for one Specific Type of Powder and With Six Individual Process Heads with Individual Water-cooled Shielding Nozzles to Each Feeder. One Six-degree of Freedom Nachi Robot for Jogging. The Process Environment is Enclosed in a Big Glove Box to Prevent Samples Being Oxidized During the Manufacturing Process.

2.2.3. Powder Feed Rate Calibration in Stage 1 and Stage 2. The wheeling feeder is used for the hybrid cell. The powder feed rate depends on the wheel rotating speed controlled by the prewrite G code saved in the computer. In the G code, the running time is set at 1 minute (adjustable) and the wheel rotating speed is controlled by the percentage of the full power sat to drive the step motor in the wheeling feeder.
By experience, the range of power is usually between 20% to 30%. By either increasing or decreasing the percentage of the motor power to adjust the real powder feed rate to be at approximately 1.8 g/min.

As the carrier gas has a negligible effect on the feed rate and we are using an open container (disposable sample tray) to collect the powder, the carrier gas is always turned at lowest to keep the powder blowing away from the collector at a minimum amount.

Zero the scaler before calibration with the sample tray is put on, so once the powder is collected the net weight of the powder can be obtained directly by weighing the collected powder and the sample tray together. Once powder weight turns to be constantly at about 1.8 g for three replicates then the feeder is calibrated, and the percentage of power set is going to be applied later to the mean code for single track deposition.

2.2.4. Geometry. The sample geometry manufactured in stage 1 & 2 is single-track thin wall to cut out MT2 micro tensile samples along build direction side by side. To extract more MT2 sample, in stage 2 the track length is increased.

2.2.4.1. Stage 1 geometry. The stage 1 of this study is focused on single track geometry of dimensions 55 mm x 2.5 mm x 15 mm. The layer thickness is 0.2 mm (75 layers). It is set up in LinuxCNC by the G code programming for tool path. Another fourth level heading. This is the second 4th level heading of Section 2. Subheadings beyond the 4th level should be avoided, and bullet points used instead. Section 3 demonstrates how to format titles that are longer than one line and how they should appear in the TOC.

2.2.4.2. Stage 2 geometry. During stage 2 of this a similar thin wall geometry samples are made but the layer thickness is increased to 0.3 mm (45 layers) to reduce oxides.

2.2.5. Tool Path. The tool paths in stage 1 & 2 are mostly the same, besides the delay in stage 1 is counted as the time taken in between the end spot of the current layer and the starting point of the next layer, the delay is counted as the time taken in between to starting points of two adjacent layers in stage 2.

2.2.5.1. Stage 1 tool path. The tool path shown in Figure 2.6. is used in stage 1 of this study. The movement is simply left and right at each height increment. At the beginning four scans, the powder feeder is programmed off, only the laser is function at the set laser power to preheat the substrate to enable a better joint of the upper build and substrate. To control the delay time and keep the gentry moving at a constant jogging speed, the gentry is programmed to move for a pre-calculated extra distance of 17 mm, so the gantry jogs left and right at the scan speed of 200mm/min to keep the 10 seconds delay time. Once the gentry jogs to the very end of each direction the gentry lowers for 0.2 mm (set up thickness) then goes back to either the left or right edge of the geometry end. Once the gentry arrives at the edge of the geometry, the deposition of the next layer starts. By repeating the above building process for 75 rounds to reach the 15 mm build height one single track thin wall sample is done.

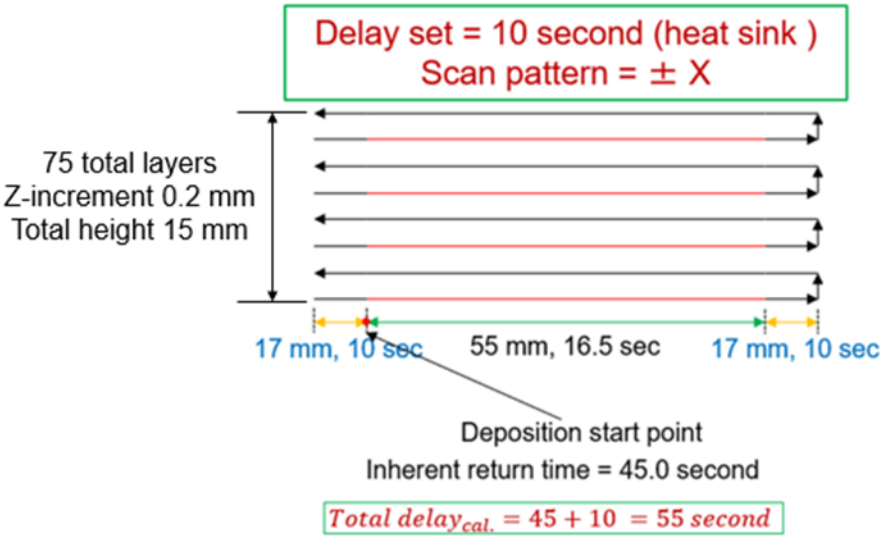

Figure 2.6 Single-track Tool Path in Stage 1. Delay Calculation: Scan Speed = 200 mm/min Travel Time = (89/200) X 60 = 26.5 Seconds Stage 1 Tool Path, During Stage 2 of This a Similar Thin Wall Geometry Samples are Made. But the Layer Thickness is Increased to 0.3 mm (45 layers) to Reduce Oxides.

2.2.5.2. Stage 2 tool path. The tool path shown in Figure 2.7 is used in stage 2 of this study. Likewise in stage 1, the laser preheat is conducted at the first four scan to enforce the binding between the upper build and the substrate. Instead of counting the delay time between the end of the current layer to the start of the next layer, the inter-layer delay time is now counted between every two starting points of two adjacent layers for better variable control as the movement of the Nachi robot is much more precise than the CNC gantry, the pose time needed to reach the set scan speed from stationary state is now negligible. In stage 2 samples are programmed to be stationary during the inter-layer delay. A 6.3 mm constant stick-out distance is applied to the entire DOE to constrain the shortest inter-layer delay time to be zero and the process to be continuous, which implies one next layer starts right after the current layer finishes.

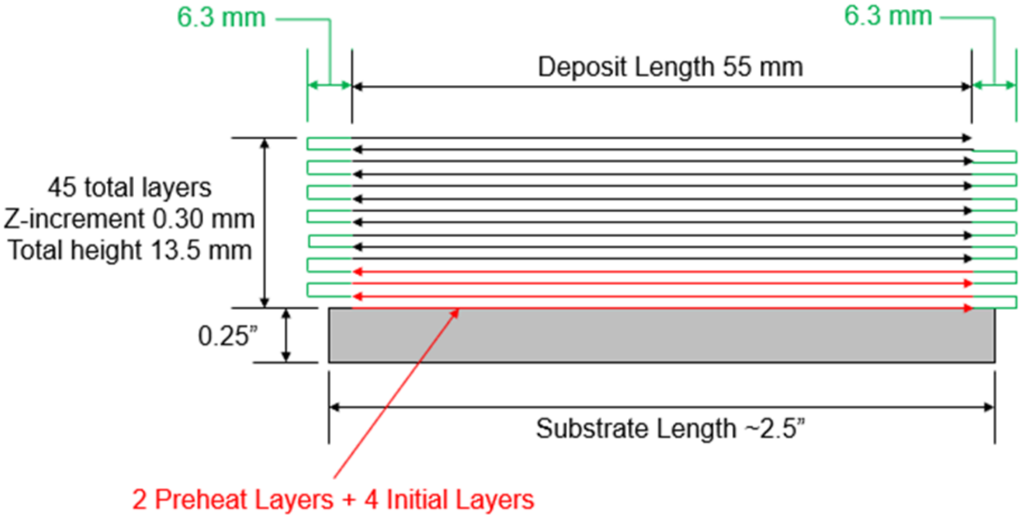

Figure 2.7 Single-track Tool Path in Stage 2.

2.2.6. Substrate. The substrates used in stage 1 & 2 are different types of steels, but in the same cross section size. The substrates of stage 2 has a longer length as the track length is longer.

2.2.6.1. Stage 1 substrate. The substrate used for AF9628 single track deposition is SS304 of a dimension of 5mm x 10mm x 55mm. As this study is mainly focused on AF9628 DED process, the substrate does not have much effect on the results at this moment.

2.2.6.2. Stage 2 substrate. To reduce the gas emission from the substrate, in stage 2 instead of using the SS304, the A36 steel is picked for its low suppletive element percentage to reduce porosity. All the A36 substrates are cut into a dimension of 0.5’’ x 0.25’’ x 2.5’’ which is about the same size of substrates used during stage 1.

2.2.7. Deposition Process. Samples in stage 1 and stage 2 are both manufactured with the DED process. Some process parameters are changed since the DED system used during stage 1 and stage 2 are different.

2.2.7.1. Stage 1 deposition process. Once the sample holder is aligned along the x-axis and leveled with the guide beam, jog the gentry to aim the guide beam right at the center of the substrate top surface. Then jog up the gentry to leave 12.5mm off set underneath the process head (copper contact tip) and jog the gentry to the right to let the process head pointing at the start point on the substrate which is about 5mm from the left edge.

Turn down the shielding gas trap (turkey bag) and seal up. Blow in argon gas at maximum flux for 10 minutes to purge down the oxygen level to 1%. Then turn down the argon supply to 10 psi and start running the single-track deposition code.

The two steps of the code are preheating and deposition, the experiment parameters in stage one is shown in Table 2.2 to proof the AF9628 powder is manufacturable with the DED process with our hybrid cell system.

The 350w laser power is used for preheating the substrate and the powder feeder is set at off. At the laser turned on, the gentry moves for 55mm to the right end and back to the start point (left end of deposition) on the left side. Stage 2 starts once the gentry moves back to the start point by the left edge. To keep the powder feed rate constant, the feeder is programmed to be non-stop during the whole 2nd stage. On the other hand, to minimize the speed variance during the direction change after each scan, the gentry is programmed to move extra 30 mm away further either past the left end or to the right end of the deposition range after each scan to ensure that the entry acceleration to be fully completed so the scan speed is constant when the deposition range is right underneath the process head. The laser is programmed to turn on at 400w when the gentry is moving between the left end and the right end of the deposition range and turns off after by-pass the two ends. The gentry is programmed to lower 0.2mm after each scan, by repeating the above process of scanning left or right for 75 times, the single-track deposition code executed and the single-track deposition sample of height 15mm is made. To avoid the sample being oxidized, it is needed to keep the argon supply on for at least 15 mins to make sure the sample cools down below the oxidization temperature before collecting the sample. And what we did during the experiment is to leave the sample in the gas trap after turning off the argon and collect the sample in overnight to be safe and to minimize the oxidization by hot sample touching the air.

Table 2.2 Single Track DED Deposition Process Parameters of Samples #1 Through #11.

Sample #	Layer width (mm)	Layer thickness (mm)	Scan Speed (mm/min)	Laser power (W)	delay (s)
1	2.5	0.2	200	350	10
2			200	400	10
3			150	300	no delay
4			200	300	no delay
5			250	300	no delay
6			150	350	no delay
7			200	350	no delay
8			250	350	no delay
9			150	400	no delay
10			200	400	no delay
11			250	400	no delay

2.2.7.2. Stage 2 deposition process. The deposition process in stage 2 is generally same as stage 1, the only difference is the parameters for the first 4 layer. The parameter of 1200 W laser power, 10.0 mm/s scan speed, 4.80 g/min powder feed rate as well as a 6-sec pause between initial and primary layers for powder feed to change are set for the first 4 layers of each sample of the entire DOE in stage 2.

2.2.8. Stage 2 Design of Experiment. The AF9628 powder is proofed manufacturable with DED process since the 11 samples are successfully made with our hybrid cell system. To further study the AF9628 tensile property, in stage 2 a 3-factor by 3-outputs central composite design of experiment (DOE) shown in Figure 2.8 (1). In total 21 single track samples are made shown in Figure 2.9 & Figure 2.10. In general, all the process parameter combinations are distributed in a 3D space in term of three individual factors. The global geometry is considered a cube outer connected to a sphere on its 8 vertices. The mean view of the 2D graph is shown in Figure 2.8 (2). One green spot two yellow spots and one blue spot is blocked by the center green spot, each red spot blocks a red spot on the back side of the cube. Each colored spot in Figure 2.8 (1) and (2) represents an individual process parameter combination. The red spots refer to box vertex, green spots refer to sphere surface which refer to critical parameters, yellow spots refer to square surface center, and blue spot refers to geometry center.

With the central composite design of experiment (DOE), the interaction of factors and the even quadratic effects can be estimated. The information from the response surface can be obtained.

The advantage of the central composite design of experiment is obvious. It is a good way to find and optimize the process settings. Also, it is a good method to troubleshoot process problems and weak points. The central composite design of experiment is also robust that the external and non-controllable influences can be drastically eliminated.

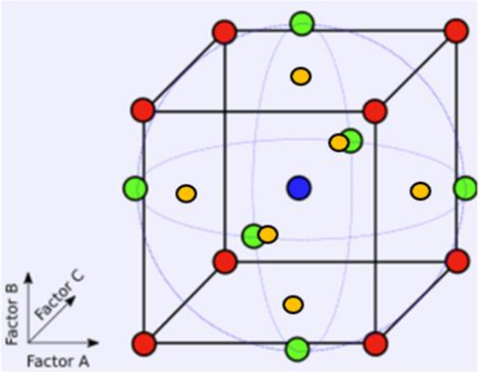

https://develve.net/Rotatable.html

(1)

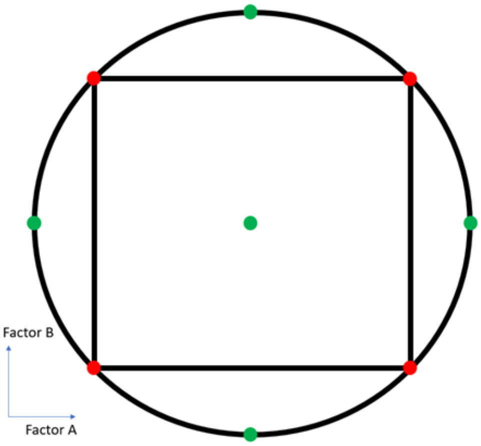

(2)

Figure 2.8 (1) AF9628 DED Process DOE in Oblique View (2) AF9628 DED Process DOE in Mean View. Each Colored Spot Represents for An Identical Process Parameter Combination. The Red Spots Refer to Box Vertex, Green Spots Refer to Sphere Surface, Yellow Spots Refer to Square Surface Center, and Blue Spot Refers to Geometry Center.

The 3 factors of laser power in walt, energy density in joule, and delay in seconds are chosen as the inputs of the DOE, referring to the three outputs of yield stress (YS) and ultra-tensile strength (UTS) in MPa, and elongation in percentage. Referring to the physical experimental feedback, the NSF system has a stable operation range of below 20 mm/s scan speed and a 500W to 1500W laser power range. The chosen input parameters are shown in Table 2.3. All critical values are labelled in red cell color. By calculating the geometry dimensions, a upper limit of 1023 W and a lower limit of 677 W are picked to bound the range of laser power variance, the 750 W 850 W and 950 W are symmetrical chosen within the laser power range. Following the same pattern, a upper limit of 124.6 J/mm and a lower limit of 55.4 J/mm are picked to bound the range of energy density variance, the 70 J/mm 90 J/mm and 110 J/mm are symmetrical chosen within the energy density range, as well as a upper limit of 18.66 s and a lower limit of 1.34 s are picked to bound the range of delay variance, the 5 s 10 s and 15 s are symmetrical chosen within the energy density range.

As shown in Table 2.4, all the DOE parameter combinations are randomized and labeled run numbers to reduce trial factors before conducting experiment.

2.3. CHARACTERIZATION

All samples in both stage 1 and stage 2 are all conducted mechanical tests, the EBSD images are taken at the selected critical results pieces form the DED manufactured AF9628 low alloy samples.

2.3.1. Polishing Process for Micro-structure Observation.

Once the micro tensile samples are tested, the broken pieces are collected and mounted with epoxy for microstructure observation. The polisher used in this study is MEPREP3 PH-3 grinding polishing system produced by Allied company. The polishing parameter used are 110 RPM for the plate and 100 RPM for the sample holder in contradict spinning directions with 10 lbs. pressing force on each sample. The surface rough finish level increases through the 600 (P-1200) fine grit silicon carbide paper, 800 (P-2400) grit silicon carbide paper, and 1200 (P-4000) grit silicon carbide paper. The samples are surface rough finished for each grit size for six minutes (2 minutes for each piece of paper). Then the polishing process went through 6-micron, 3-micron, 1-micron, and 0.05-micron polycrystalline diamond suspension. Eight minutes are spent on each level of the samples with also 10 lbs. of the pressing force and ultrasonic wash between each grit size of the polishing suspension. Once the samples are done with the 0.05-micron polishing suspension and ultra-sonic washed up, ethanol is sprayed on to push away the residual water to keep the polished surface from being oxidized. Once the ethanol natural dried up, the polished samples' surfaces are wiped up by lens tissue. In this procedure, the samples are polished for the microstructure observation with the SEM.

During stage 2, the parts between two adjacent MT2 pieces adjacent to the MT2 specimens tested critical tensile results among yield stress, ultimate tensile strength, or elongations are selected and polished with the same process for grain analysis.

2.3.2. Micro-structure (How SEM Images Are Taken). After polishing the samples to 0.02 micron, the SEM images are taken under the BES-COMPO mode to investigate the surface information of sample 1 and sample 2. After the first SEM observation, the samples are etched by 2% nital for 80 seconds for a clearer surface microstructure. The parameters set for single polished sample 1 are 25 kV acceleration voltage, SP 5, WD 10.2, at 2.5k magnification, and for polished sample 1 after etching are 15 kV acceleration voltage, SP 10, WD 10.3, at 1.0k magnification. For sample 2 the parameters are set for single polished at 15 kV acceleration voltage, SP 7, WD 6.7, at 2.0k magnification, and for polished and etched are 15 kV acceleration voltage, SP 10, WD 10.8, at 910 magnifications. Both sample 1 and sample 2 are investigated by EDS mode for element mapping as well for more surface element composite information in respect to the tensile results.

Table 2.3 Chosen Input Parameters in Stage 1 DOE. All Critical Values are Labelled in Red Cell Color. Parameters of Each Factor Are Central Symmetrically Chosen Within Each Range.

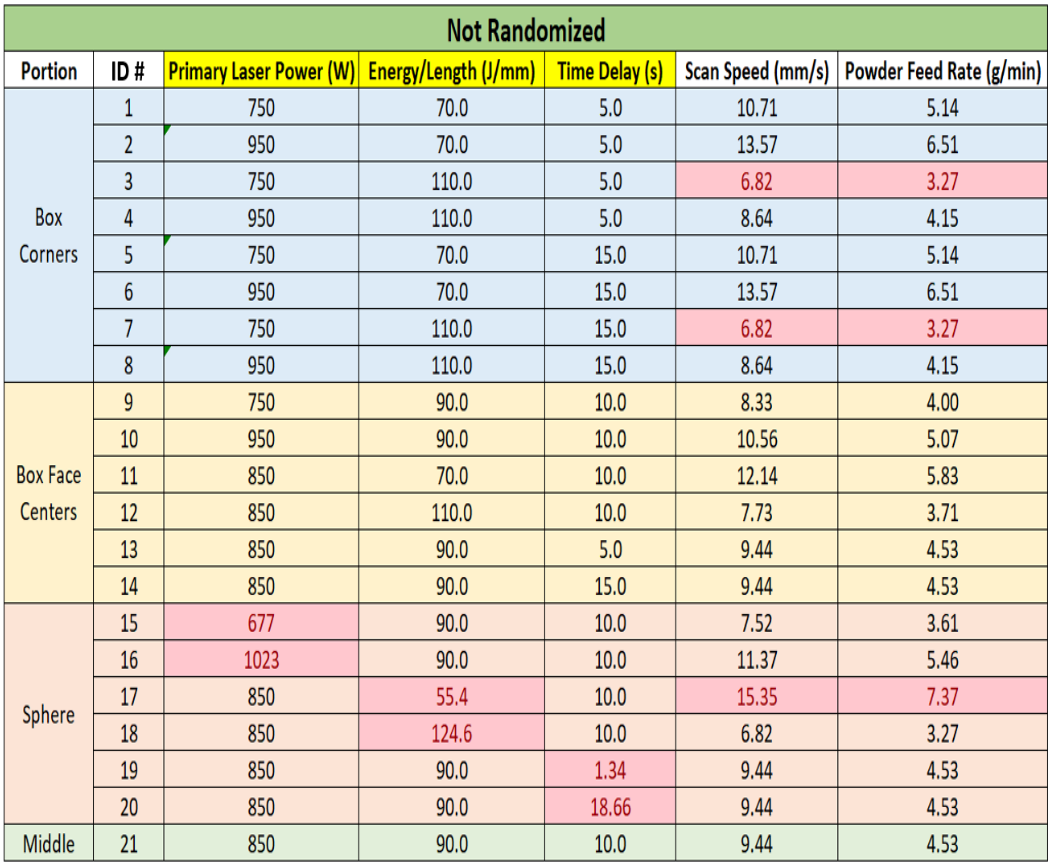

Not Randomized						
Portion	ID #	Primary Laser Power (W)	Energy/Length (J/mm)	Time Delay (s)	Scan Speed (mm/s)	Powder Feed Rate (g/min)
Box Corners	1	750	70.0	5.0	10.71	5.14
	2	950	70.0	5.0	13.57	6.51
	3	750	110.0	5.0	6.82	3.27
	4	950	110.0	5.0	8.64	4.15
	5	750	70.0	15.0	10.71	5.14
	6	950	70.0	15.0	13.57	6.51
	7	750	110.0	15.0	6.82	3.27
	8	950	110.0	15.0	8.64	4.15
Box Face Centers	9	750	90.0	10.0	8.33	4.00
	10	950	90.0	10.0	10.56	5.07
	11	850	70.0	10.0	12.14	5.83
	12	850	110.0	10.0	7.73	3.71
	13	850	90.0	5.0	9.44	4.53
	14	850	90.0	15.0	9.44	4.53
Sphere	15	677	90.0	10.0	7.52	3.61
	16	1023	90.0	10.0	11.37	5.46
	17	850	55.4	10.0	15.35	7.37
	18	850	124.6	10.0	6.82	3.27
	19	850	90.0	1.34	9.44	4.53
	20	850	90.0	18.66	9.44	4.53
Middle	21	850	90.0	10.0	9.44	4.53

Table 2.4 Randomized Input Parameters in Stage 1 With Labelled Run Numbers.

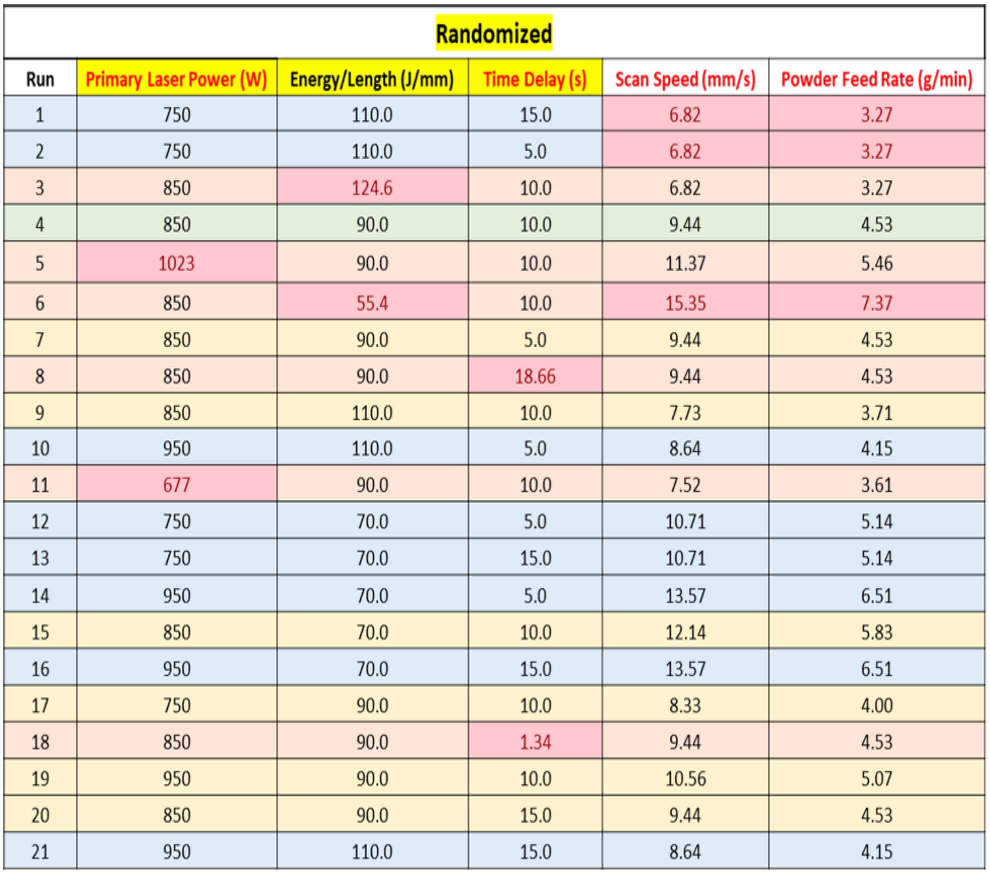

Randomized					
Run	Primary Laser Power (W)	Energy/Length (J/mm)	Time Delay (s)	Scan Speed (mm/s)	Powder Feed Rate (g/min)
1	750	110.0	15.0	6.82	3.27
2	750	110.0	5.0	6.82	3.27
3	850	124.6	10.0	6.82	3.27
4	850	90.0	10.0	9.44	4.53
5	1023	90.0	10.0	11.37	5.46
6	850	55.4	10.0	15.35	7.37
7	850	90.0	5.0	9.44	4.53
8	850	90.0	18.66	9.44	4.53
9	850	110.0	10.0	7.73	3.71
10	950	110.0	5.0	8.64	4.15
11	677	90.0	10.0	7.52	3.61
12	750	70.0	5.0	10.71	5.14
13	750	70.0	15.0	10.71	5.14
14	950	70.0	5.0	13.57	6.51
15	850	70.0	10.0	12.14	5.83
16	950	70.0	15.0	13.57	6.51
17	750	90.0	10.0	8.33	4.00
18	850	90.0	1.34	9.44	4.53
19	950	90.0	10.0	10.56	5.07
20	850	90.0	15.0	9.44	4.53
21	950	110.0	15.0	8.64	4.15

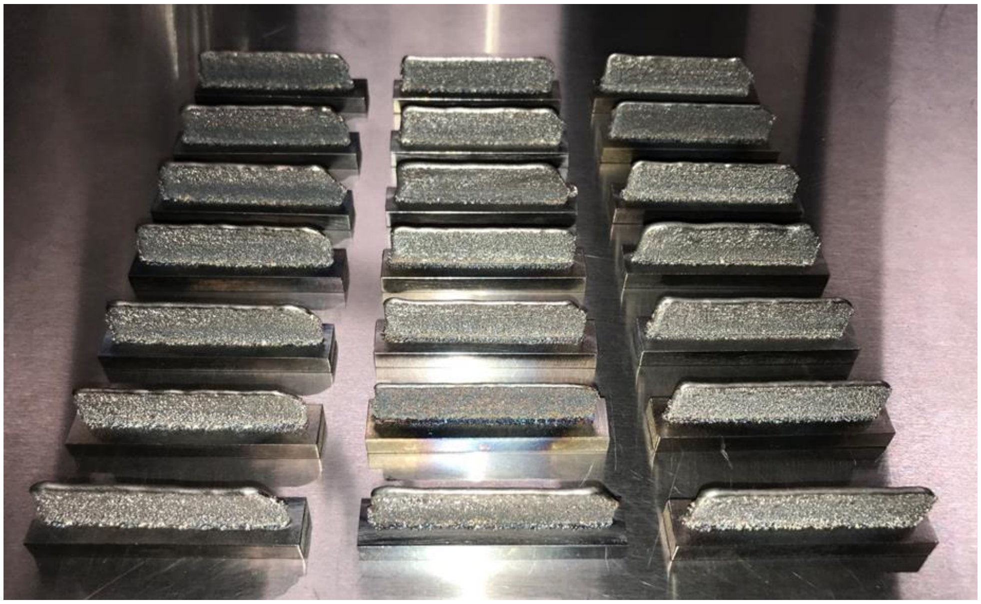

Figure 2.9 21 DOE Samples in Stage 2 for Tensile Tests.

Figure 2.10 One of the 21 Single-track DOE Samples in Stage 2.

2.4. MECHANICAL TESTING

Tensile tests are done to find out the tensile of samples made during stage 1 and stage 2.

2.4.1. Micro-tensile Sample Preparation.

Since the rust remainder from EDM cut effects the thickness measurement, all micro-tensile samples are processed before conducting mechanical tests for higher accuracy.

2.4.1.1. Brief process.

In both Stage 1 and 2, once the sample is deposited, we sliced the single-track deposition as well as the substrate vertically with EDM into 1 mm thickness pieces. Then fix the piece horizontally to cut 6 to 9 micro tensile samples side by side out of the piece. Rough finish (polish) with 800 grit sandpaper to remove the surface oxide, take the measurement with the micrometer, and record the dimensions of the micro-tensile sample. Repeating the process for all pieces, once the sample dimension table is made, then the samples are prepared.

2.4.1.2. EDM cutting theory. The electric discharge manufacturing (EDM) machine is good at cutting conductive metals. The EDM we are using is Hansvedt model DS-2 traveling wire EDM. There are two discharge poles in the machine; one is connected to the vise, and the other one is connected to the part of the traveling wire. Once the sample is fixed on the vise, a gap of approximately 20 um between the sample and the wire should be reminded by jogging the sample either away from or towards the wire. During the cutting process, a high AC voltage is applied across the two discharge poles. The electric current break through the air across the gap in the meantime generates electric sparks of a fairly high temperature which vaporizes the sample close to the wire. In the meantime, the sample keeps moving toward the wire, hence the cutting process continues.

2.4.1.3. Slicing. Firstly, we mounted our single-track sample vertically to cramp the substrate onto the EDM vise, to let the sample height direction along the y axis, jog the EDM wire along x axis to the left side, until the wire barely touches the sample right surface. Then jog the wire to -y direction and stop jogging as soon as the wire get off the sample surface (10 to 20 um gap). Since the thickness of the single-track geometry is around 1.7 to 1.3 mm, jog further left for 0.15 mm then start cutting towards +y direction until cutting across both the sample surface and the substrate. Once done cut, jog the wire back along -y direction to the starting point. Due to the DEM cutting theory being based on using high-temperature sparks, it is unavoidable that the residual heat on the cut across section causes oxidization on the sample surfaces. Hence a thickness of slightly over 1mm is needed. As the wire diameter is 0.3 mm, jog 1.3 mm along -y direction so the 0.3

off set is reserved. Then by one more straight cut along +y direction one approximately 1.1mm thickness piece is made. Show in Figure 2.11(a).

2.4.1.4. Micro-tensile sample cut out. After the slice is obtained, we cut the micro tensile samples side by side out of the approximately 1.1mm thick piece. Since the focus of this study is AF9628 additive manufacturing process parameters, 7 micro tensile samples along the z direction are cut out from each sample upper built side by side, the joint of substrate and deposition is not included in the samples at this moment. The program we used to cut the samples is “DOGBONEC”, the 0.3 mm offset is included, the accuracy is ± 20 um. The micro tensile sample dimension is shown in Figure 2.11(b).

2.4.1.5. EDM cutting parameters. The cutting parameters are pulse (millisecond) 1, percentage on-time 1.5, peak amplitude 10, gap space 1, servo speed 3, cut off 1.

2.4.1.6. Surface rough finish. As mentioned above, due to the DEM cutting unavoidable that the residual heat on the cut across section causes oxidization on the sample surfaces. Hence a thickness of slightly over 1 mm is needed for the following surface rough finish (polishing) process. As the work distance is less than 50 um and the sample size is small, what we did is just to stick one piece of 800 grit sandpaper onto the table then press one piece of the done cut micro-tensile sample with the finger on the sandpaper, drawing circles in both clockwise and counterclockwise directions until the shining surface reviles on a side then flip the micro-tensile sample and repeat the process for the other side of the piece cutting parameters. The cutting parameters are pulse (millisecond) 1, percentage on-time 1.5, peak amplitude 10, gap space 1, servo speed 3, cut off 1.

(a)

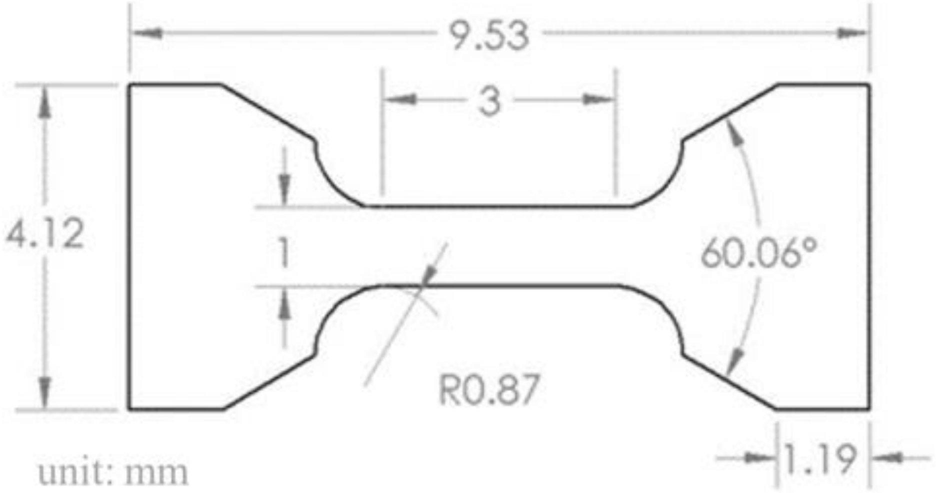

(b)

Figure 2.11 (a) The Locations Where the Micro-tensile Samples Are Extracted From a 1mm Thick Slice (b) The Dimensions of the Micro-tensile Samples.

unavoidable that the residual heat on the cut across section causes oxidization on the sample surfaces. Hence a thickness of slightly over 1 mm is needed for the following surface rough finish (polishing) process. As the work distance is less than 50 um and the sample size is small, what we did is just to stick one piece of 800 grit sandpaper onto the table then press one piece of the done cut micro-tensile sample with the finger on the sandpaper, drawing circles in both clockwise and counterclockwise directions until the shining surface reviles on a side then flip the micro-tensile sample and repeat the process for the other side of the piece cutting parameters. The cutting parameters are pulse (millisecond) 1, percentage on-time 1.5, peak amplitude 10, gap space 1, servo speed 3, cut off 1.

2.4.1.7. Sample dimension measurement. Once the oxides on both sides of the sample are worn off, we took the measurement on the precise width and thickness of each micro-tensile sample. Identically, for each dimension of each piece of micro-tensile sample we measured it for three times to take the average of the three measured numbers, then make the averaged width and thickness measurements as well as the 3mm default length into a table referring to each piece of the micro-tensile samples for the next-step tensile test. The micrometer we are using is “Mitutoyo 293-340-30” It has an accuracy of three decimal places.

2.4.2. Tensile Test. All MT2 samples during stage 1 & 2 are micro tensile tested for yield stress, ultimate tensile strength, and elongation to refer to process parameters.

2.4.2.1. Tensile tester & test parameters. The tensile tester we used in both stages in this study is “INSTRON” accompanied with an ex-tensile meter and “Bluehills3” control program. It has a 50 kN maximum stress which is way more than enough for our micro tensile sample. The tensile test parameters we used are 0.015mm/mm/min test speed and 1.5mm/min rate 2.

2.4.2.2. Tensile test process. Once the software is ready, for each deposition we firstly created a folder including several files referring to number of micro tensile samples of this deposition. From the very left piece to the very right piece, the files and pieces are numbered by 1 through the last (either 6 or 7). Then referring to the sample dimension table mentioned above during sample preparation, default the sample length at 3mm, type in the sample width and thickness of each piece of micro tensile sample and double check. Select the file 1 and load the left most piece of micro tensile sample into the sample holders with a tweezer and push the piece to the middle of the sample holder with a T shape calibrator. After taking off the calibrator, turn on the sample protecting mode and jog the upper grasp up to increase the load to approximately 60 N. Then off sample protecting mode, cramp on the extensile meter across the sample holder and pull off the safe pin of the ex-tensile meter and start the tensile test by click on the start button in the Bluehills3 program. The data measured by the sensor is plotted and shown synchronously by the Bluehills3 program, once the maximum yield stress (YS) is obtained the pulling process pauses and the reminder pops up. Take off the ex-tensile meter and insert the safe pin back in it, by clicking on ok to resume the test until the micro tensile sample being pulled to break for ultimate tensile stress as well as maximum elongation at break. After collecting the pulled-up piece, the file 1 completes. By repeating the process to test on all the prepared pieces to obtain the tensile results of the depositions.

2.4.3. Stage 1 Hardness Testing Procedure. After the micro-tensile samples are tested, the debris are collected and prepared (shown in Figure 4b) for Vickers-hardness test. The hardness tester used in this study is “Struers Duramin5” shown in Figure 4a).

On each piece of debris, three locations shown in Figure 2.12(c) are put along a perpendicular direction (x-axis) to the build direction on the wide end of each piece, three indents are put at each location to calculate the local mean hardness value. In total, twelve locations (36 indents) of each sample are tested for the global hardness value. All indents are tested by the parameters set at 9.81N 10 seconds and 40x magnification shown in Table 3.5.

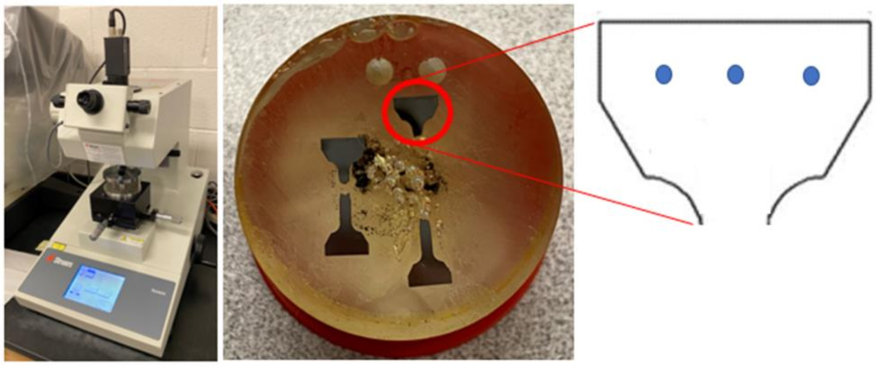

(a) (b) (c)

Figure 2.12 (a) “Struers Duramin5” Vickers-hardness Indenter Used in This Study (b) Four Pieces of Prepared Micro-tensile Debris of Sample 2 in One Epoxy Mounted for Hardness Test (c) Three Vickers-hardness Tested Locations on One Piece of Micro-tensile Debris Labeled in Blue Color.

3. RESULTS AND DISCUSSION

3.1. STAGE 2 POWDER EDS ANALYSIS

The AF9628 low alloy powder we used in this study is the commercial AM powder produced by Powder Alloy Corporation. The AF9628 particle composite is analyzed by the EDS. The powder images shown in Figure 3.1. are taken from epoxy mounted AF9628 powder after being polished to exposes cross area. As shown in these images, the AF9628 powders we purchased for this study are not perfectly spherical. [13] [14] Some of the particles are in an elliptical shape. Iron element contributes to over 90% of the element composition. The element signals are shown in Figure 3.2.

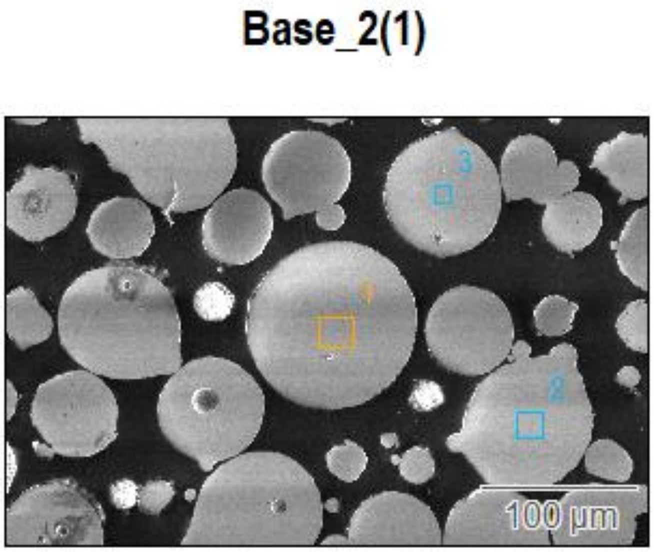

Image Name:	Base_2(1)
Image Resolution:	2048 by 1364
Image Pixel Size:	0.20 µm
Acc. Voltage:	5.0 kV
Magnification:	999

Figure 3.1 Three Spots Tested on Polished Powder Cross Area and Testing Parameters.

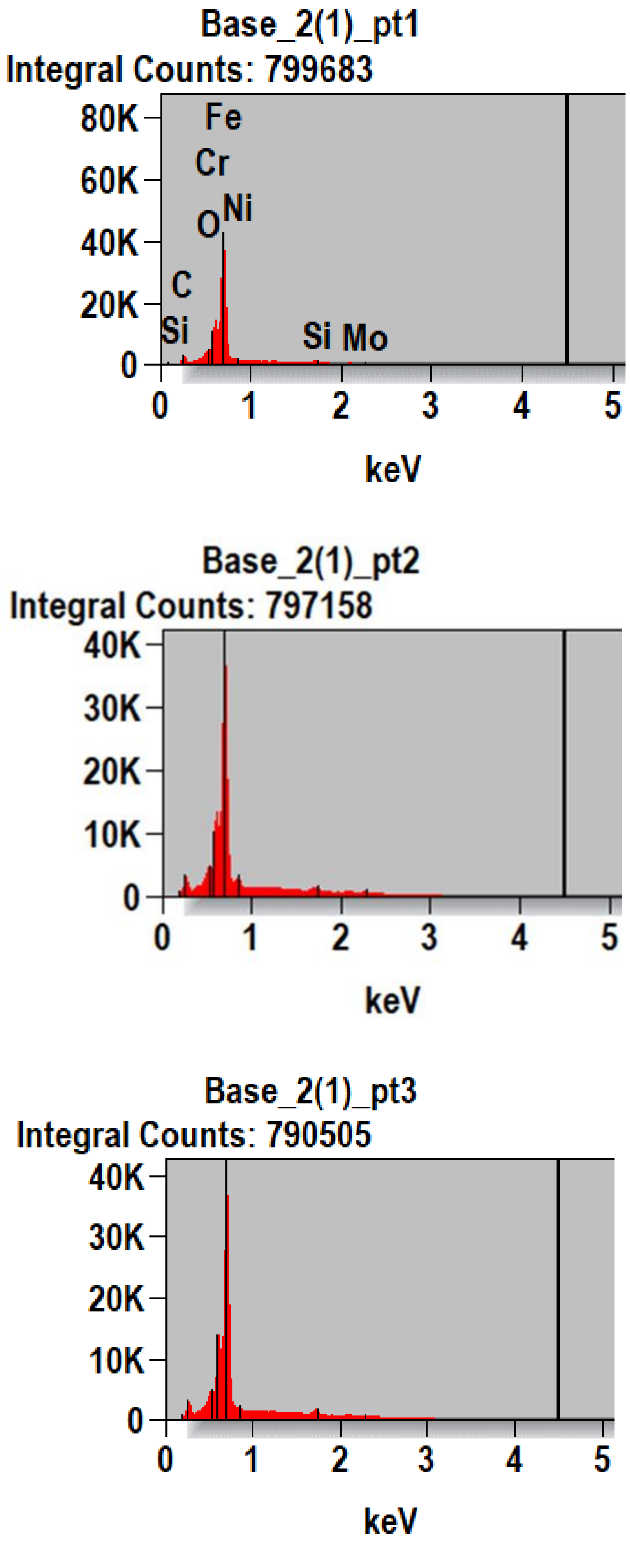

Figure 3.2 Element Signals Out of the Three Tested Spots.

3.2. STAGE 1 & 2 IMAGE ANALYSIS

The sample images are taken from the samples tested critical tensile results during the stage 1 and stage 2 with SEM for surface defect analysis.

3.2.1. Stage 1 Images. The selected samples in stage 1 are analyzed for surface micro-structure. SEM images are taken for surface analysis BSE-Compo process.

3.2.1.1. Stage 1 SEM & BSE-Compo images. A clean surface contrast is expected to be observed, however as the AF9628 is a type of low alloy, extremely limited surface information is collected. However, some lath shape microstructures are observed (shown in Figure 3.3) around some features of sample 1. In addition, the atomic mass distribution across the polished surface is uniform as the uniform brightness in BSE-COMPO is shown in Figures 3.3 and 3.5. By analyzing the SEM images, a uniform surface under backscatter compo mode is observed at both sample 1 and sample 2, which states that there is not a critical composition difference across the polished area (shown in Figures 3.4 and 3.6). This point is agreed by the feedback from the EDS element mapping in the later study in SEM. Also, the uniformly distributed element map agrees with the element distribution of either as-pint or after heat treatment in the study [3] However, the element distribution of the as-built samples in the study [4] is not as uniformly distributed as what we observed in our study. The process in our study is DED, but the element distribution from our study is uniform and more like the element distribution of SLM process.

3.2.1.2. Effects of parameters in microstructure. Based on the above analysis, the difference in defect density caused by process parameters should be the major factor of sample 1 and sample 2 obtaining different tensile results. Since the laser power is the only difference in sample 1 and sample 2 process parameters. Lack of fusion (shown in Figure 3.7) is more likely to happen in sample 1, and the mean factor of sample 1 tested lower UTS than sample 2 should be its higher density of cracks due to lack of fusion.

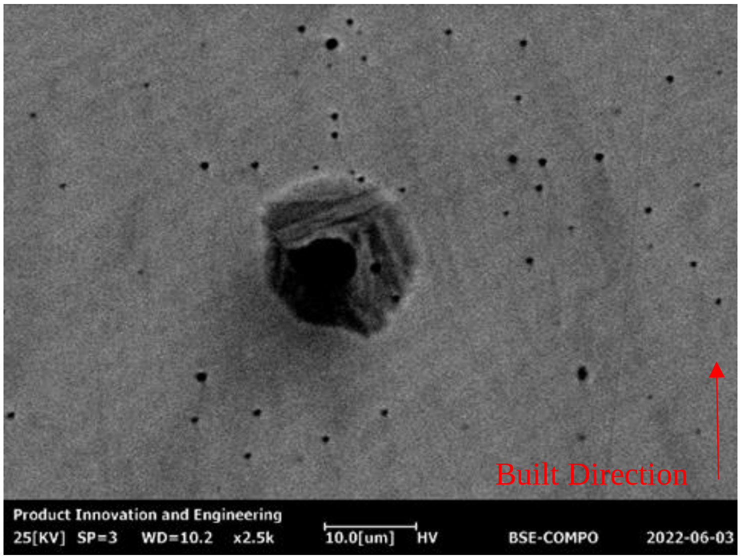

Stage 1 Sample 1 Polished BSE-Compo Image.

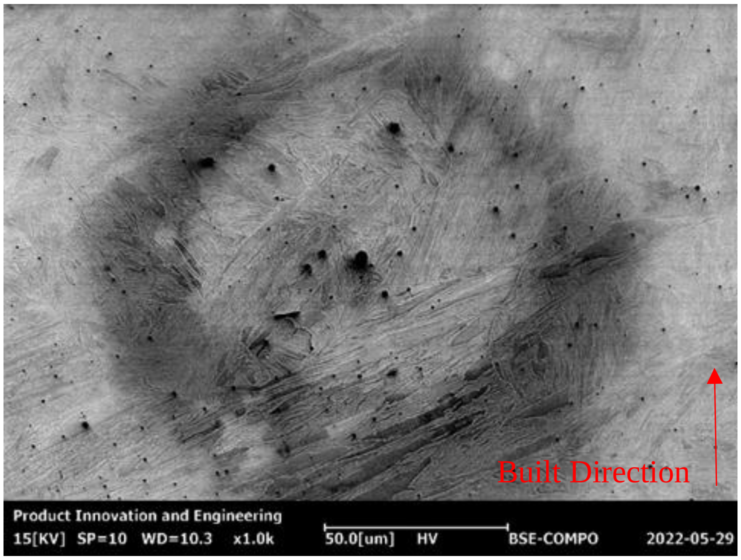

Stage 1 Sample 1 Polished and Etched BSE-Compo Image.

Figure 3.3 SEM Images of Sample 1 in BES-COMPO Mode Etched and Non-etched at Different Locations.

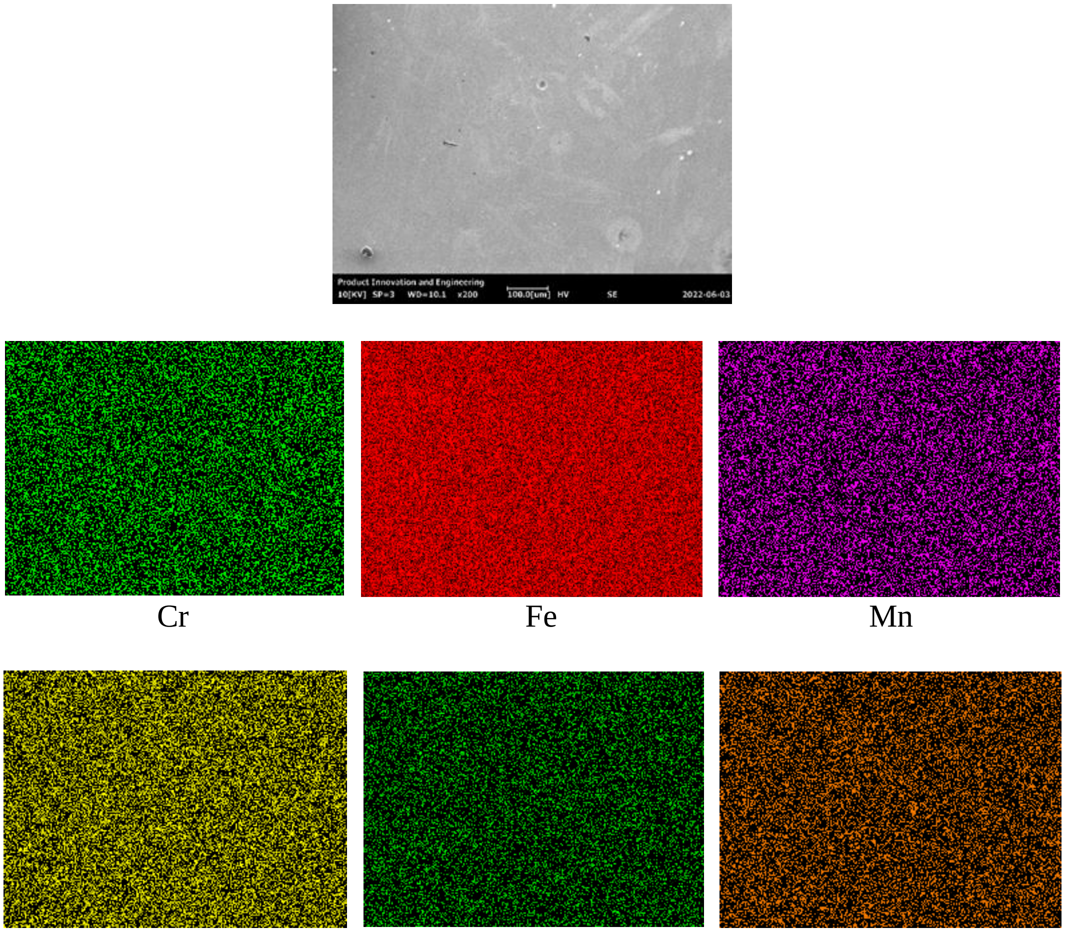

Cr Fe Mn

Mo Ni V

Figure 3.4 Partial Elements Mapping of Sample 1.

3.2.2. Stage 2 Images. All the selected samples for EBSD analysis have been polished through the same polishing steps as mentioned above. The SEM FSD images are shown below in Figure 3.8 through 3.11. No obvious defects are seen at sample #8 Max UTS or sample #15 Max elongation. Two spherical pore defects are seen on sample #5 Min UTS and sample #13 Min elongation. The finest surface is seen at sample #13. The sample #5 has the most brightness contrast comparing with the other three images which implies it to be a relatively coarse surface. Some hump shape features are seen at sample #15.

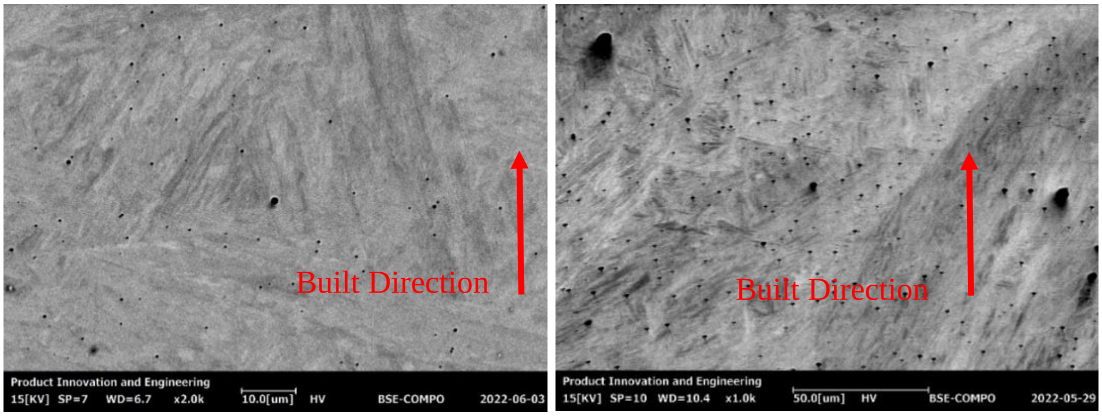

Figure 3.5 SEM Images of Sample 2 in BES-COMPO Mode Etched and Non-etched at Different Locations.

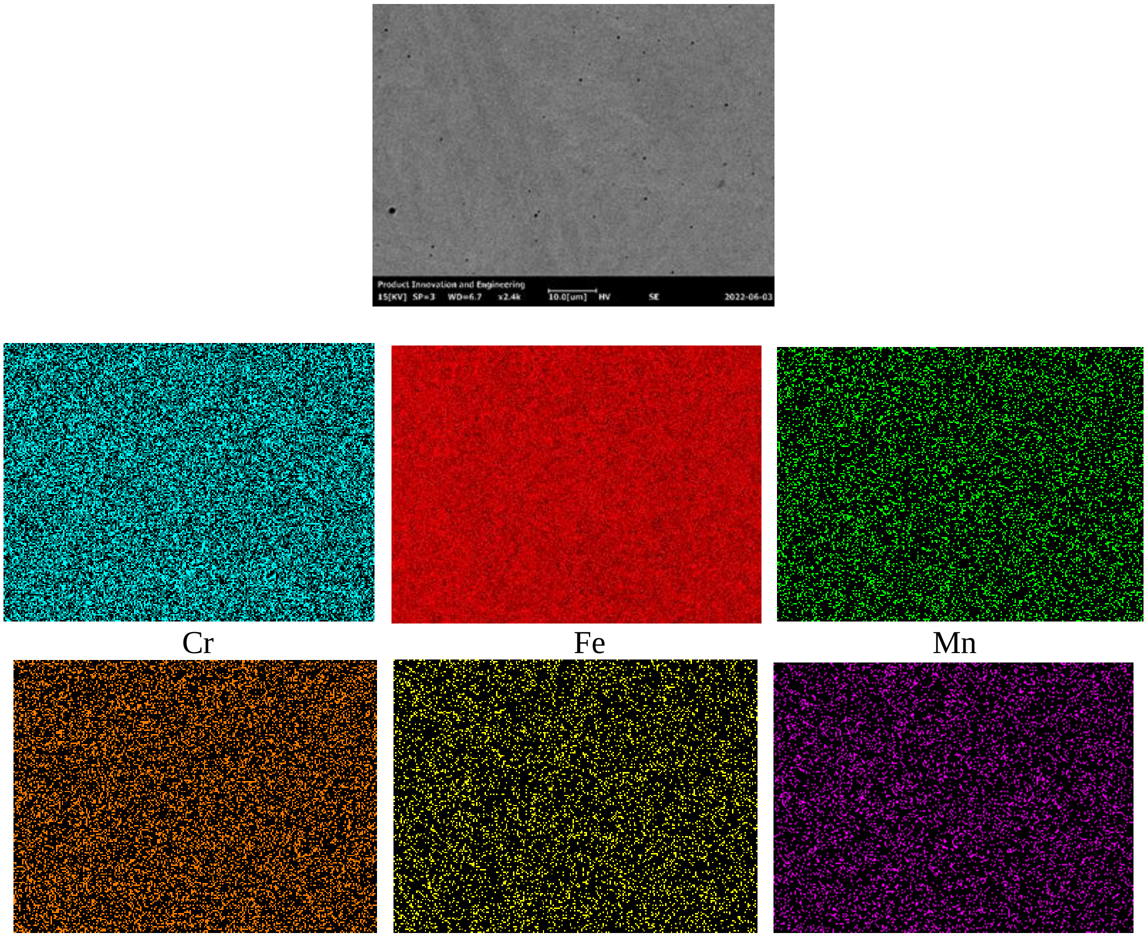

Cr Fe Mn

Mo Ni V

Figure 3.6 Partial Elements Mapping of Sample 2.

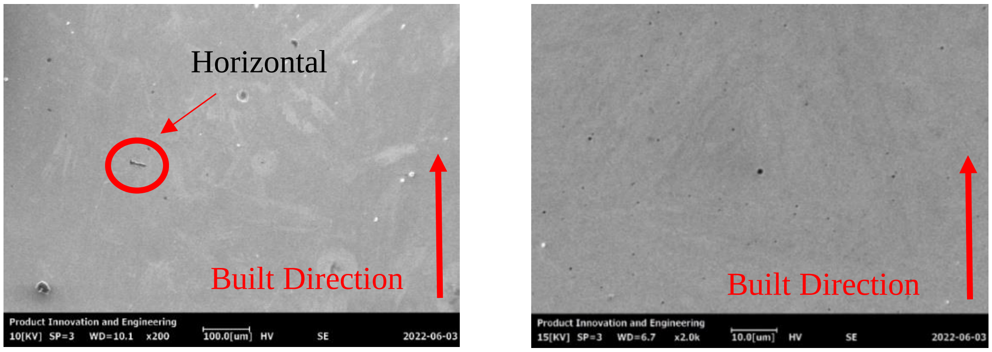

Figure 3.7 Defect Density Comparison of Sample 1 & 2. Defect Due to Lack of Fusion is Seen at Sample 1.

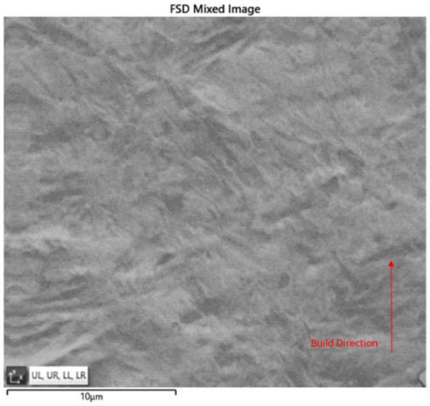

Figure 3.8 DOE Sample #8 Max UTS EBSD Fore Scattered Detector (FSD) Images for Phase Analysis.

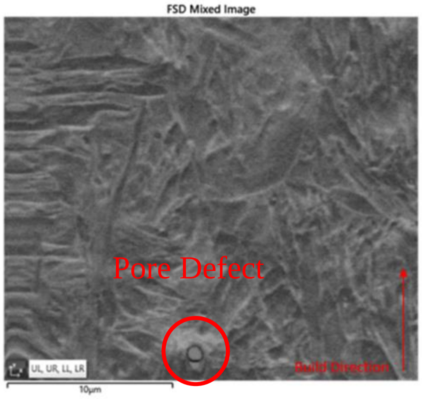

Figure 3.9 DOE Sample #5 Min UTS EBSD Fore Scattered Detector (FSD) Images for Phase Analysis.

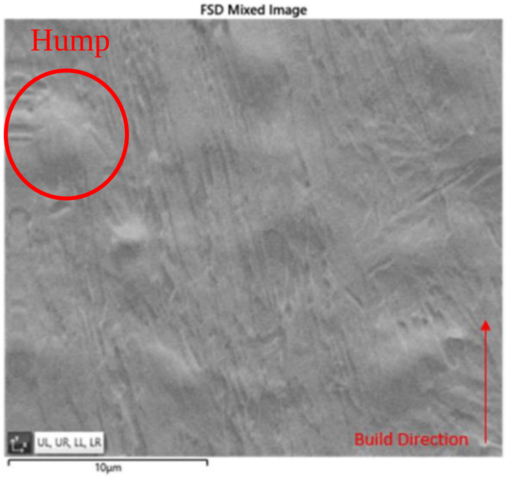

Figure 3.10 DOE Sample #15 EBSD Max Elongation Fore Scattered Detector (FSD) Images for Phase Analysis.

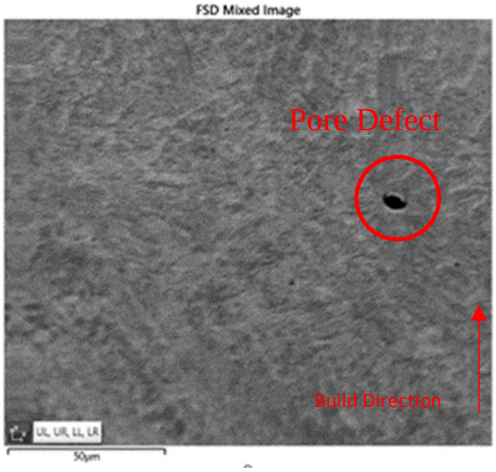

Figure 3.11 DOE Sample #13 EBSD Min Elongation Fore Scattered Detector (FSD) Images for Phase Analysis.

3.3. MICROSTRUCTURE

All samples with critical tensile results are analyzed with EBSD for grain morphology. All grain sizes are tested small which implies the cooling rate during the manufacturing process is relatively high.

3.3.1. Stage 1 Microstructure (SFF). The porosity morphology shown in Figure 3.12 sample 1 could indicate lack of fusion defects as the irregular defects are observed. In Figure 3.12 sample 2 the porosity is evenly distributed, which could indicate outgassing in this higher energy density specimen.

As what is shown in Figure 3.13, the phase mappings of sample 1 and 2 are showing different phase morphologies. Comparing with sample 2 the phases size of sample 1 are more uniform.

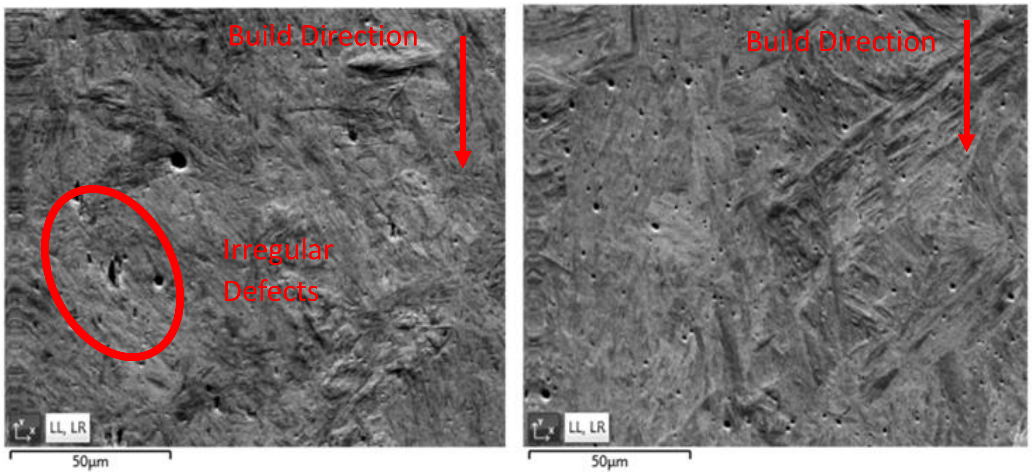

Stage 1 Sample 1 Stage 1 Sample 2

Figure 3.12 Sample 1 & 2 EBSD Fore Scattered Detector (FSD) Images for Porosity Comparison.

In this study, ferrite and cementite phases are specifically focused to find Bainite. As what is shown in Table 3.1, assuming the total carbon content of both samples is similar, the lower rate of a discrete carbide phase in sample 2 could indicate a higher prevalence of bainite than in sample 1. Potentially more austenite phases are transformed into Bainite during the transforming stage of the cooling process in sample #2.

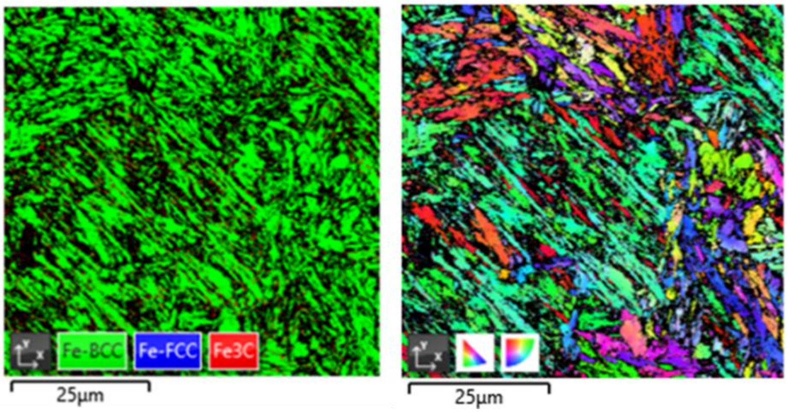

Stage 1 Sample 1 Stage 1 Sample 2

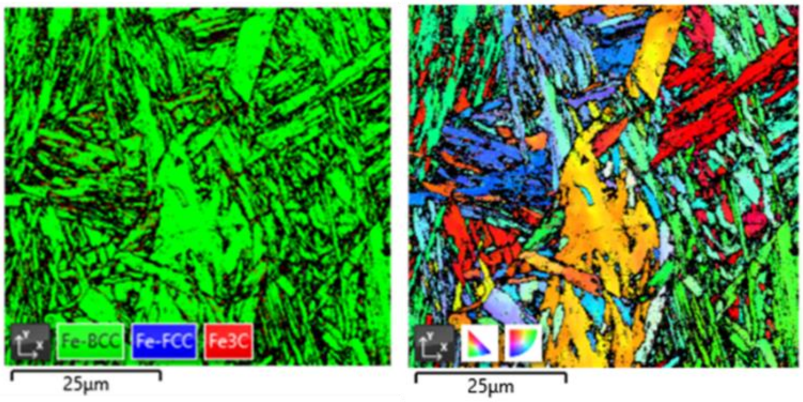

Stage 1 Sample 2 Phase Color Stage 1 Sample 2 IPF Color

Figure 3.13 Sample 1 & 2 Phase Mappings for Phase Size Comparison.

Table 3.1 DED Sample 1 And 2 Mapping Analysis

	Sample 1		Sample 2	
Phase Name	Phase Fraction (%)	Phase Count	Phase Fraction (%)	Phase Count
Fe-BCC	49.67	97025	59.18	99581
Fe-FCC	0.25	497	0.29	485
Fe3C	4.53	8846	2.95	4959
Zero Solutions	45.55	88971	37.59	63245
Median [µm]	1.5		0.9	

* Mean grain diameter analyzed with phases over 10 pixels

Sample 2 highest frequency bin shown in Figure 3.14 is the sub-micron category, indicating that the median grain size is much smaller than sample 1. The smaller median grain size in sample #2 supports the tensile result of sample #2 is tested a higher UTS than sample #1 [13].

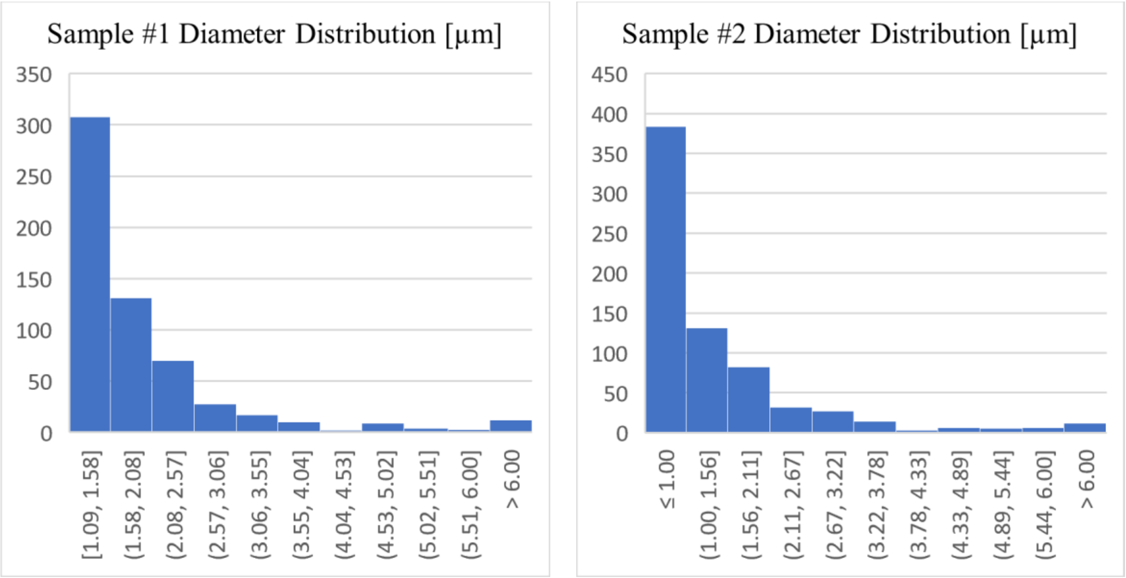

Figure 3.14 Stage 1 Sample #1 & #2 Grain Diameter Distributions [µm].

3.3.2. Stage 2 Microstructure. All the following EBSD images are taken with Helios, all phase fractions and average grain sizes are analyzed in Aztec Tango and Channel 5 software with grains over 100 pixels.

As it is shown in Figure 3.15 and Table 3.2. The grain size of sample #5 has smaller grain size and variance in grain size than sample #5. The grain orientation of sample #8 is mostly between along 101 and 111, grains’ edges and corners are mostly exposed to the polished surface along the z direction of the coordinate. In sample #5 the grains’ orientation is mostly concentrated in between 001 and 111 along x and z direction of the coordinate, mostly grains' surfaces and corners expose to the polished sample surface.

As it is shown in Figure 3.15 and Table 3.2. Most DOE sample #5 grains formed more randomly comparing with sample #15 with some bigger size grains are seen cross over the analyzed area. Based on the inverse pole figure shown in Figure 3.15 #8. Observing from the x direction, the grains embedded cross over the analyzed area mostly expose lattice surfaces and corners to the polished surface as the multiple uniform distribution in x direction mostly close to the direction 001 and 101. The grain directions are less condensed along the y direction comparing with the x or z direction inverse poles, but the grains mostly expose surfaces and corners as the concentration of grain orientations are closer to direction 001 and 111. From the z direction, the grains embedded cross over the analyzed area mostly expose corners to the polished surface as the multiple uniform distribution in z direction mostly close to the direction 111.

As it is shown in Figure 3.15 sample #15 and Table 3.2. The majority of DOE sample #15 grains formed vertically which is along the build direction cross over the analyzed area. Based on the inverse pole figure shown in Figure 3.15 #15. Observing from the x direction, the grains embedded cross over the analyzed area mostly expose edges to the polished surface as the multiple uniform distribution in x direction mostly close to the direction 101. From the y direction, the grains embedded cross over the analyzed area mostly expose corners to the polished surface as the multiple uniform distribution in x direction mostly close to the direction 111. The grain directions are less condensed along the z direction comparing with the x or y direction inverse poles, but the grains mostly expose corners as the concentration of grain orientations are closer to direction 111.

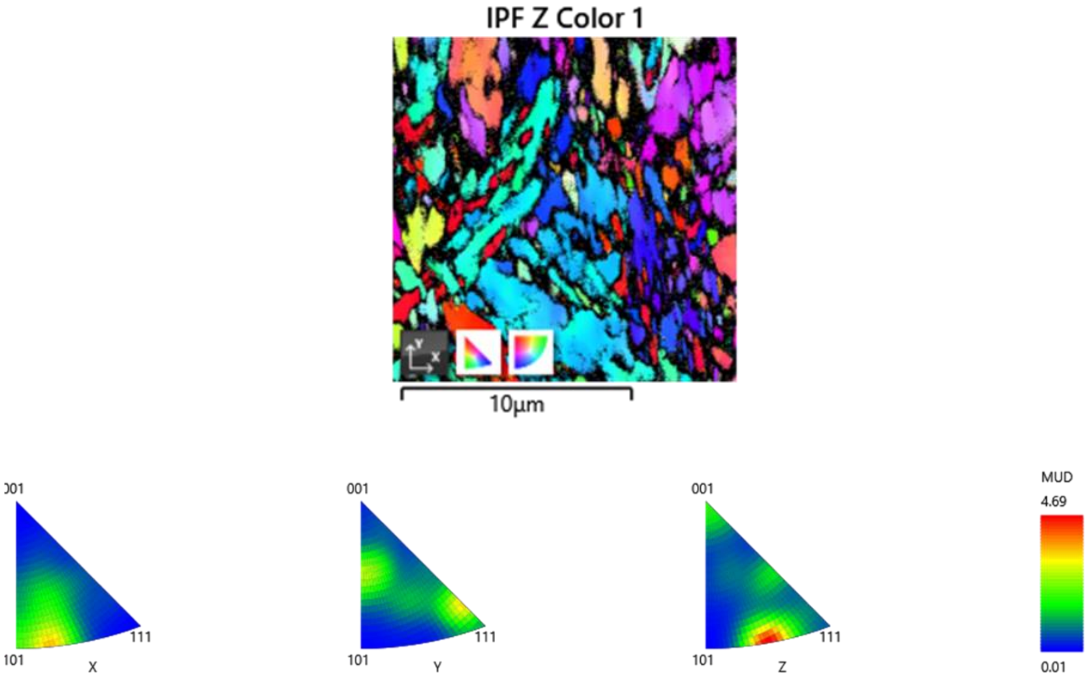

Sample #8 Max UTS

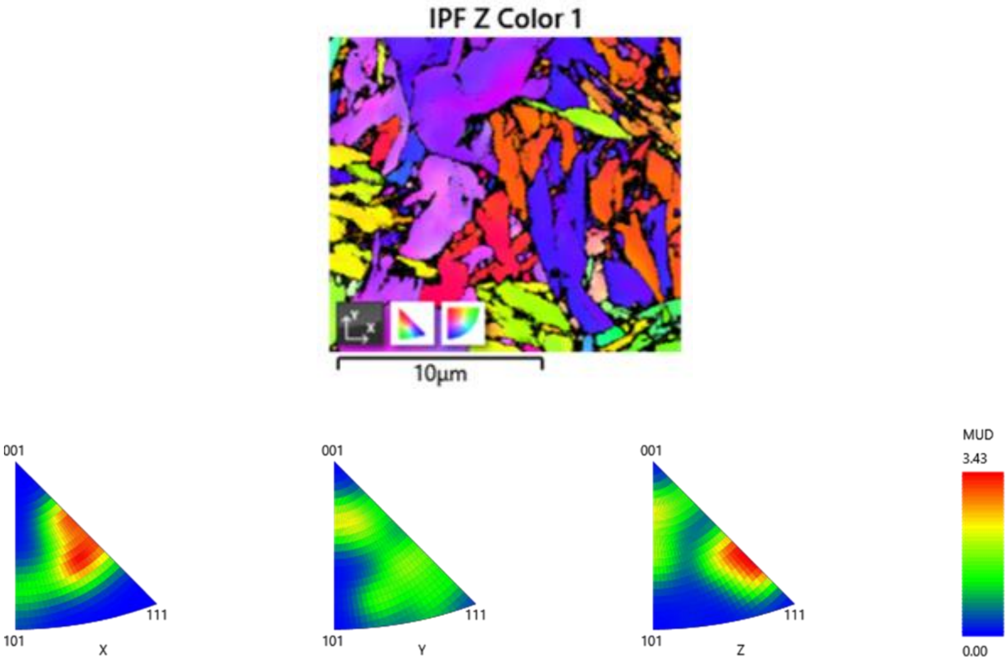

Sample #5 Min UTS

Figure 3.15 Critical Tensile Results IPF Images.

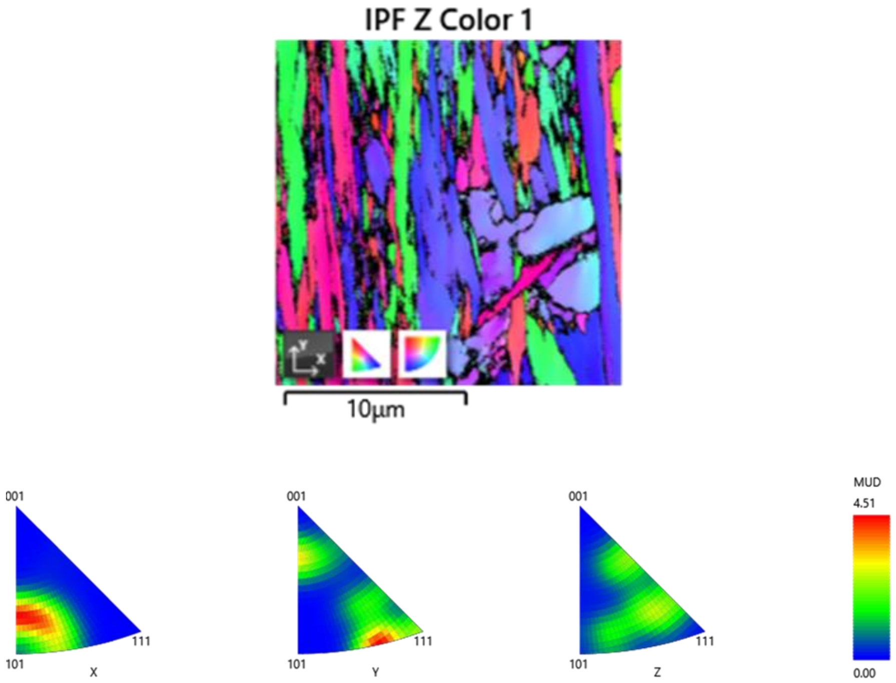

Sample #15 Max Elongation

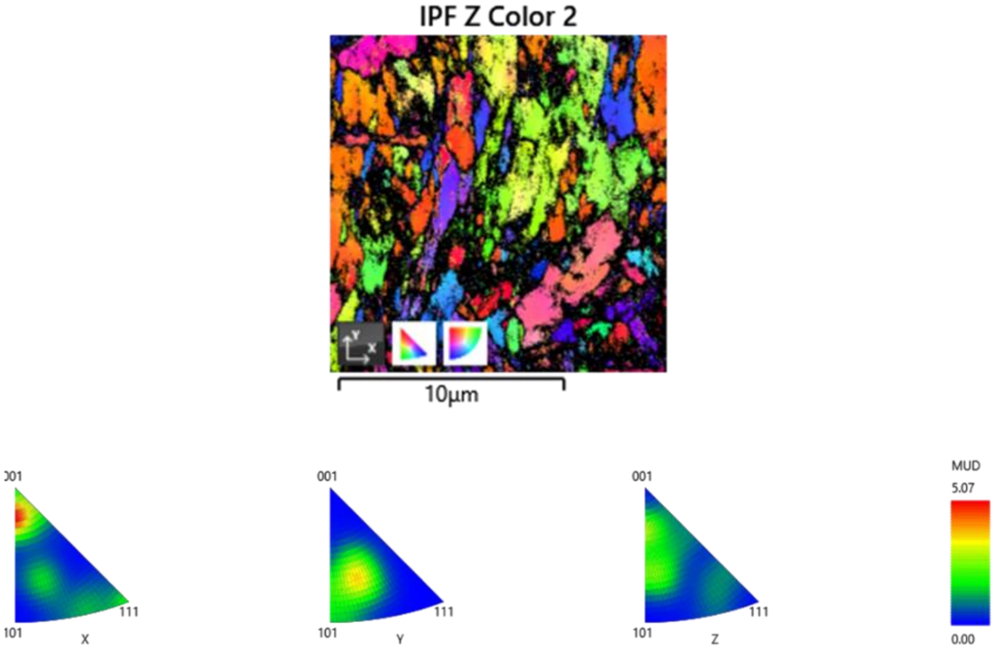

Sample #13 Min Elongation

Figure 3.15 Critical Tensile Results IPF Images. (cont.)

The phases shown in Figure 3.16 and Table 3.2. Sample #15 are mostly Fe-BCC phase. Fe-FCC and Fe3C phases are rarely observed. The phases shown on sample #5 are mostly Fe-BCC phase. Fe-FCC and Fe3C phases are rarely observed. In sample #5 the Fe3C is detected at much higher level than the other samples. The solution area of sample #8 and #5 are tested 20% lower than sample # 5 and sample #15. The solution areas are tested lower than 80% as the grain size of all the samples are small due to the high cooling rate. The grains are not able to grow big as the sample temperature exceed the forming range over fast.

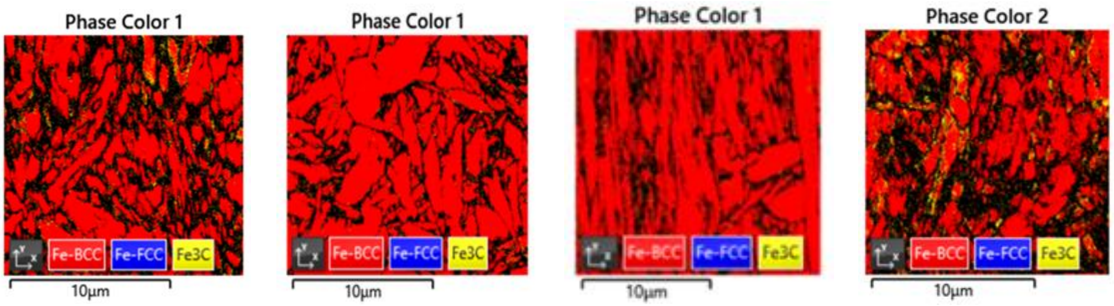

#8 Max UTS #5 Min UTS #15 Max Elongation #13 Min Elongation

Figure 3.16 Critical Tensile Results Phase Mapping.

Table 3.2 UTS & Elongation Critical Average Grain Size & Non-zero Solution Area Percentage (Analyzed based on non-border grains with over 100 pixels)

	#8 Max UTS	#5 Min UTS	#15 Max Elongation	#13 Min Elongation
Ave. Grain size (um)	0.90248	1.4875	1.1177	0.9512
S.D.	0.51335	1.0689	0.65911	0.85564
Non-zero Solution Are (%)	57.95	75.5	76.53	54.14
UTS (MPa)	1733.92	1395.02	1579.75	1681.76
Elongation (%)	22.2	23	23.4	6.8
Energy / Length (J/mm)	90.0	90.0	70.0	70.0
Time Delay (s)	18.66	10.0	10.0	15.0

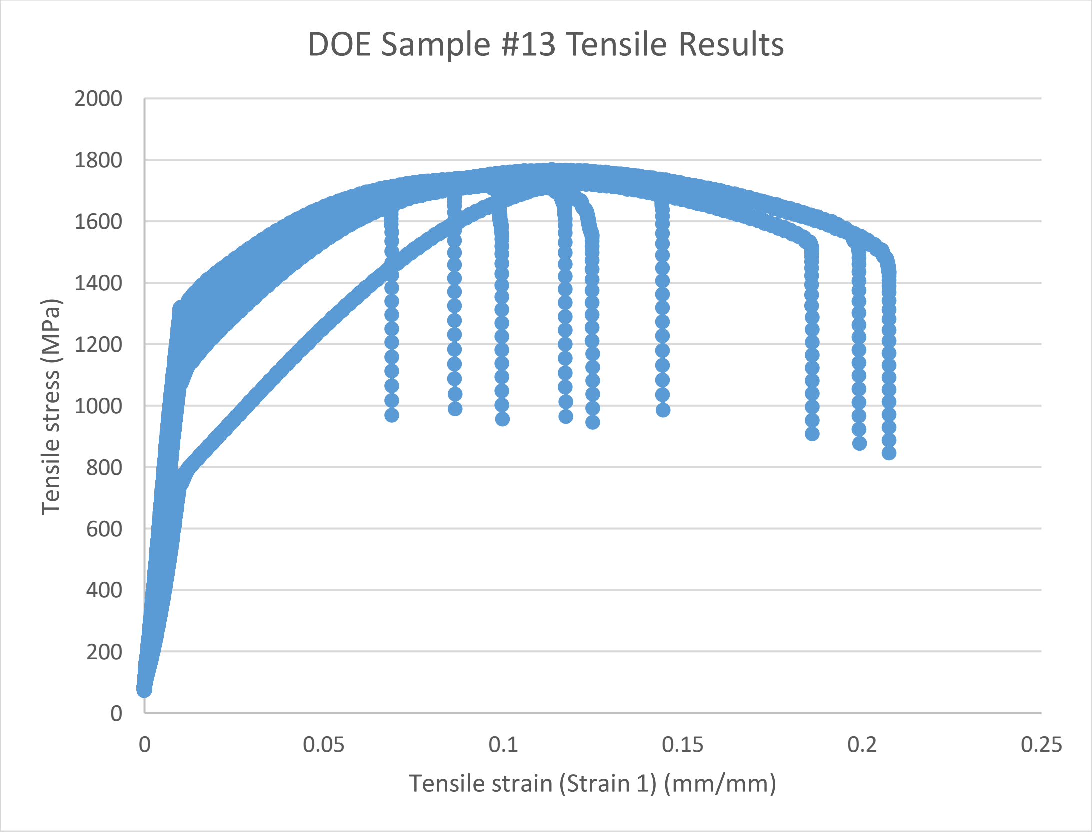

Figure 3.17 DOE Sample #13 Include the Min Elongation Record

3.4. TENSILE PROPERTIES

The three aspects of the yield stress, ultimate tensile strength, and elongation are meanly focused on this study. All samples are tested relatively high UTS and elongation.

3.4.1. Stage 1 Micro-tensile Results Analysis. Eleven samples are tested under the same tensile test parameters in this study. Both sample 1 and sample 2 are deposited at 200 mm/min and 10 seconds delay between each layer, but sample one is processed with 350 W laser power, and sample two is processed with 400 W laser power. The tensile results of sample 1 and sample 2 are shown in Figures 3.18, 3.19 and compared with other tensile results in Table 3.4.

3.4.1.1. Sample 1 vs. sample 2. Sample 1 and 2 are both tested for over 900 MPa yield strength and a relatively high elongation of over 20% [14] [15]. Sample one is tested slightly higher than sample 1 based on the calculated mean YS values and mean elongation percentages. However, a mean ultra-tensile strength of over 1800 MPa is tested in sample two, which is about 400 MPa (28%) higher than sample 2.

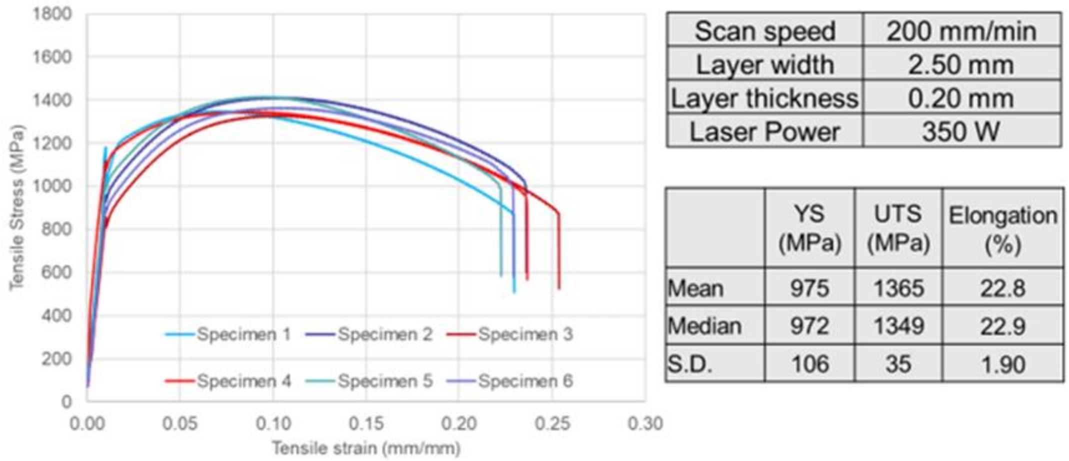

Scan speed	200 mm/min
Layer width	2.50 mm
Layer thickness	0.20 mm
Laser Power	350 W

	YS (MPa)	UTS (MPa)	Elongation (%)
Mean	975	1365	22.8
Median	972	1349	22.9
S.D.	106	35	1.90

Figure 3.18 Stress-strain Curve Process Parameters and Tensile Results of Sample 1, 200 mm/min Scan Speed, 10s Delay Between Each Layer 350 W Laser Power.

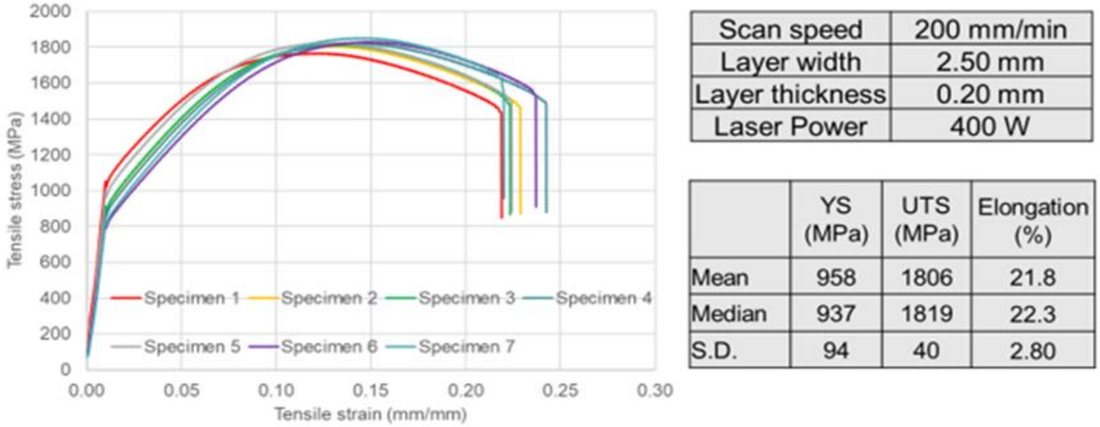

Scan speed	200 mm/min
Layer width	2.50 mm
Layer thickness	0.20 mm
Laser Power	400 W

	YS (MPa)	UTS (MPa)	Elongation (%)
Mean	958	1806	21.8
Median	937	1819	22.3
S.D.	94	40	2.80

Figure 3.19 Stress-strain Curve Process Parameters and Tensile Results of Sample 1, 200 mm/min Scan Speed, 10s Delay Between Each Layer 400 W Laser Power.

3.4.1.2. DED samples without delay at 300W, 350W, 400W. The sample deposited with no delay between each layer are shown in Figure 3.20 (a) through (c). None of the nine consciously deposited samples is tensile tested for an over 1600 MPa UTS or an over 15% elongation. Sample #5 and sample #11 tested a mean UTS value close to 1500 MPa. Relatively uniform elongation percentages are tested on the no delay samples. The elongation range is between 6% to 8%. The yield strength distribution is tested around 1000 MPa, and the highest mean yield strength is tested 1100 MPa at sample #5.

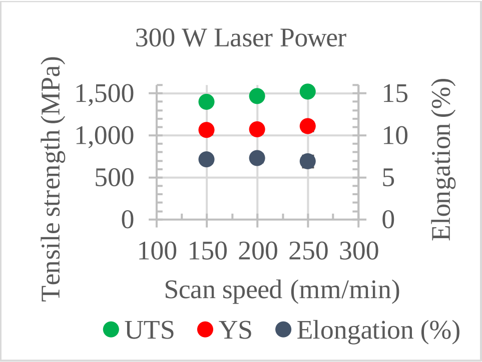

Figure 3.20 (a) Tensile Test Results from No Delay Samples of 300W Laser Power at Different Scan Speed.

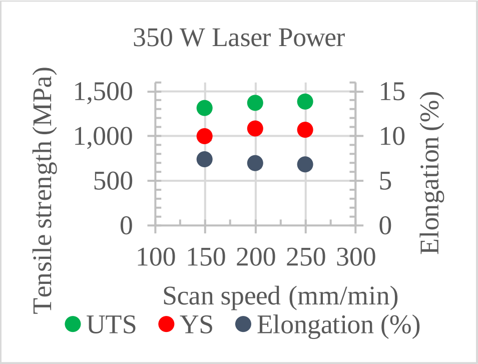

Figure 3.20 (b) Tensile Test Results from No Delay Samples of 350W Laser Power at Different Scan Speed.

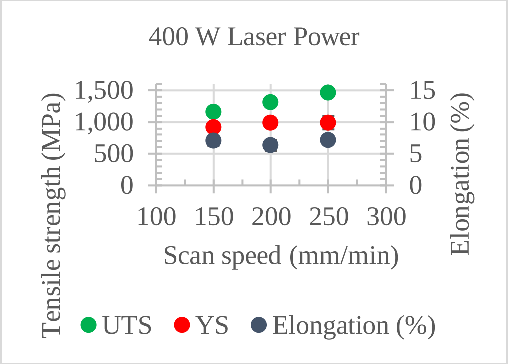

Figure 3.20 (c) Tensile Test Results from No Delay Samples of 400W Laser Power at Different Scan Speed.

3.4.1.3. DED samples with 10s delay vs. cast. Sample one and sample two tested relatively the same yield strength as the cast AF9628 steel shown in Figure 3.21, and the UTS of sample 1 is tested relatively the same as the cast AF9628. However, the UTS of sample 2 is 400 MPa higher than the UTS of the cast AF9628, and both sample 1 and sample 2 are tested about 7% higher than the cast AF9628 in mean elongation.

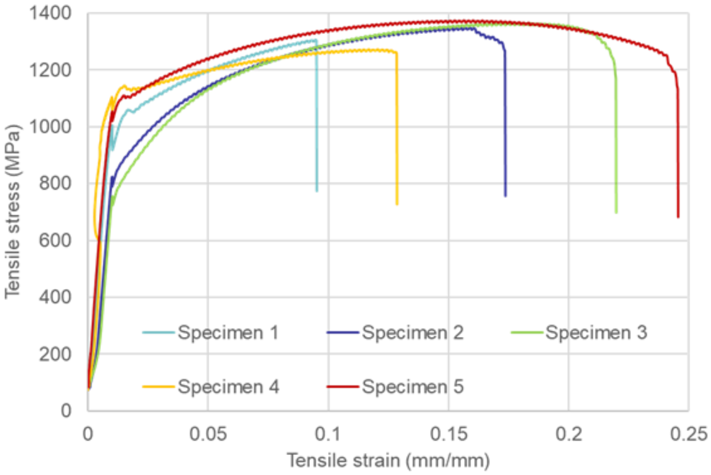

	YS (MPa)	UTS (MPa)	Elongation
Mean	978	1339	15.4
Median	983	1356	15.0
S.D.	150	41	7.10

Figure 3.21 Cast AF9628 Stress-strain Curve and Tensile Results.

3.4.1.4. DED samples with 10s delay vs. SLM literature review. Sample one deposited in this study is tested about 100 MPA lower in YS compared with the SLM processed AF9628 tested at both vertical direction and horizontal directions. However, the UTS of the SLM processed AF9628 is about 100 MPa lower than sample 1 and 500 MPa lower than sample 2., and the mean elongation of sample one and sample two are both 50% high than the SLM processed AF9628 compared with [#1] shown in Table 3.3.

The YS in [#2] shown in Table 3.3 is about 500 MPa higher than either sample 1 or sample2, and the UTS of [#2] is 300 MPa higher than sample 1 but 100 MPa lower than sample 2 in all tested directions. However, the elongation of sample 1 and sample 2 are both about twice of the elongation percentage of the [#2] results in all directions.

Table 3.3 AF9628 SLM Process Tensile Results From [6]

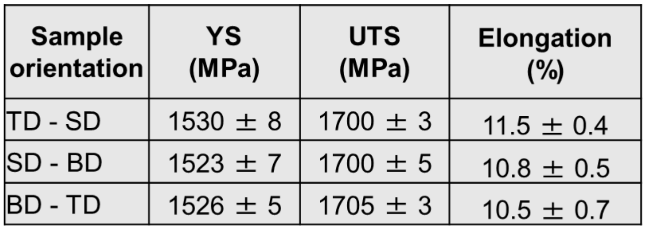

Sample orientation	YS (MPa)	UTS (MPa)	Elongation (%)
TD - SD	1530 ± 8	1700 ± 3	11.5 ± 0.4
SD - BD	1523 ± 7	1700 ± 5	10.8 ± 0.5
BD - TD	1526 ± 5	1705 ± 3	10.5 ± 0.7

Table 3.4 AF9628 Tensile Comparison of Different Processes in Energy Density, Ultra-tensile Strength, Yield Strength, and Elongation.

Processes	ED (J/mm^3)	UTS (MPa)	YS (MPa)	Elongation (%)
DED (No Delay)	144	1517	1105	6.9
DED (10 S Delay)	240	1806	958	21.8
Cast	n/a	1339	978	15.4
SLM [5]	Not given	1700	1530	11.5
SLM [6]	60.1	1420	1100	7.71

3.4.1.5. Sample 1 and sample 2 fracture surface SEM image analysis. The ductile fracture surfaces shown in Figures 3.22(a)(b) and 3.22(a)(b) are observed at both sample 1 and sample 2. No sign of brittle surface is observed at sample 1 or sample 2. Sample 1 and sample 2 have a similar surface texture at x500 magnification. The overview at low magnification of sample 1 fracture surface is observed to be finer and slightly more uniform than the overview of sample 2 fracture surface. However, a larger pore defect is seen at the corner of sample 1 fracture surface. Sample 1 had a higher defect density than sample 2, which resulted in sample 2 being tested with a much higher UTS than sample 1 in the tensile test.

Because of the stress more likely accumulates at the defects, the more defects the more likely the stress will find a breakthrough to cause tensile failure. On the other hand, a more uniform body has more capability to sustain stress as the stress is going to be distributed more evenly and less likely to accumulate throughout the entire body.

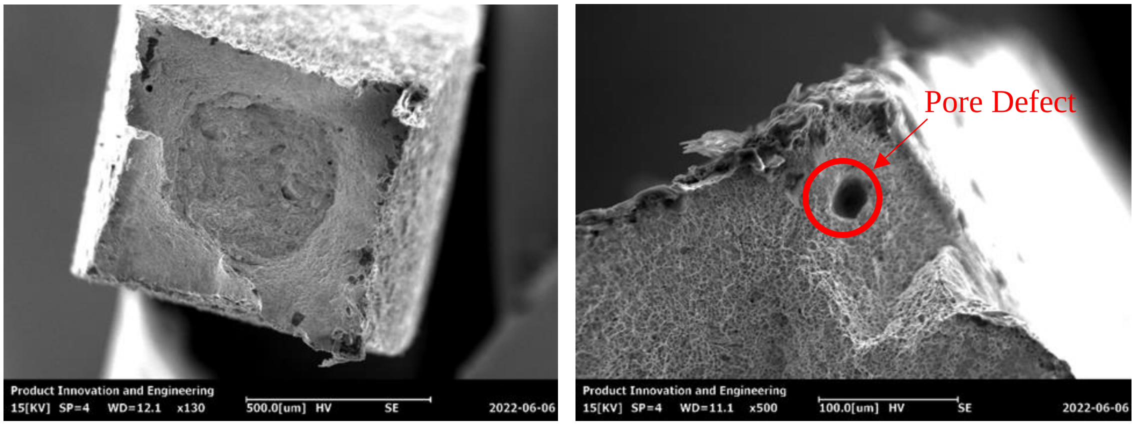

(a) (b)

Figure 3.22 (a) Sample 1 Fracture Surface SEM Image at x130 Magnification Overview (b) x500 Magnification at the Conner of the Fracture Surface.

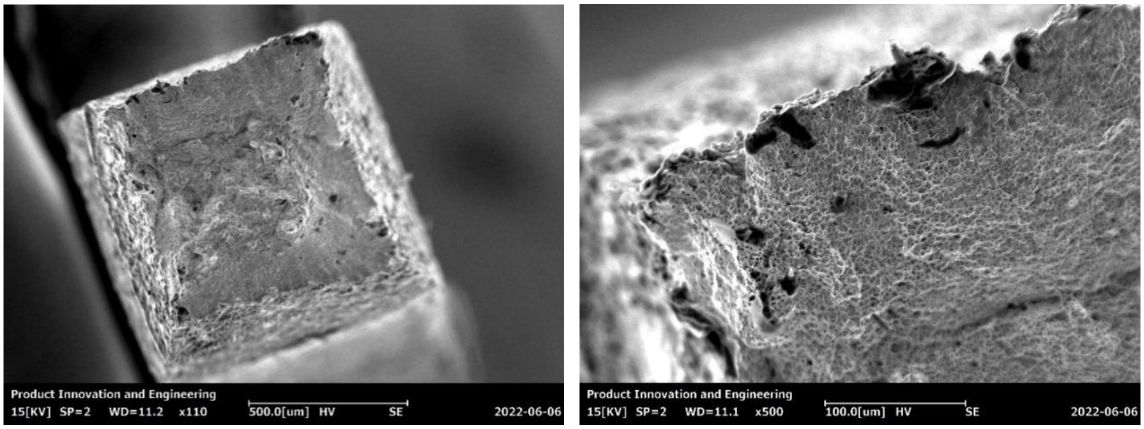

(a) (b)

Figure 3.23 (a) Sample 2 Fracture Surface SEM Image at x110 Magnification Overview (b) x500 Magnification at the Corner of the Fracture Surface.

3.4.2. Stage 2 DOE Micro-tensile Results Analysis (Trendlines & P Values).

The focused design of experiment is conducted during stage 2. In total 21 DOE specimens are manufactured with the DED process. 168 pieces of MT2 samples out of the 21 DOE specimens are tested for micro tensile properties at room temperature. The tensile results obtained from the 21 DOE specimens are analyzed in JMP Pro 16 software. As shown in Figure 3.24 through 3.36, 21 linear fit models individually in terms of yield stress (YS) in mega Pascha, ultimate tensile strength (UTS) in mega Pascha and elongation in percentage, versus laser power in watt, energy density in joule per millimeter, inter-layer delay in seconds as well as the crossed factors are generated. The yield stress has flat trend lines referring to either single factors or crossed factors. In single factor fit models, in most of the cases the inter-layer delay affects the trends of UTS positively but the elongation negatively however some of the cases have both high UTS and relative high elongation. The laser power or energy density has positive effect to the elongation but negative effect to the UTS.

3.4.2.1. Single factors. Based on the DOE results using linear fit models shown in Figure 3.24 through 3.26, the yield strength appears to be less effected by the parameters than the UTS or elongation. All three plots in terms of yield stress individually versus laser power, energy density, and inter-layer delay are showing flat trend lines as the parameter levels change. The probability values are significantly greater than 0.05, all the 3 hypotheses of laser power, energy density, and inter-layer delay referring to yield strength are null.

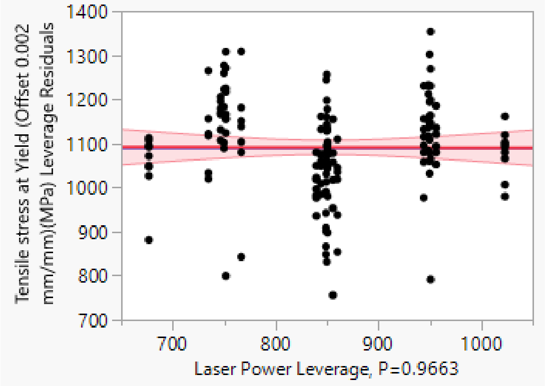

Figure 3.24 Yield Stress in Mega Pascha vs. Laser Power in Watt. The Trend Line Slope ≈ 0, The Probability Value Is Significantly Greater Than 0.05.

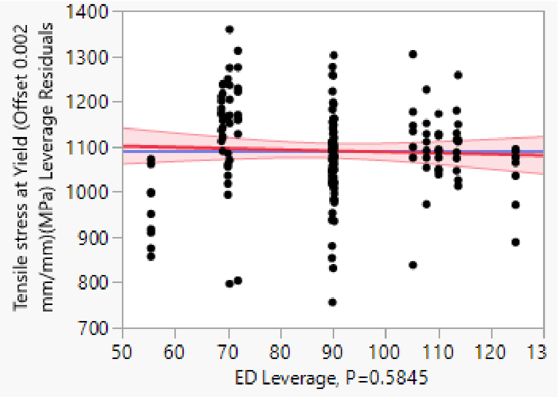

Figure 3.25 Yield Stress in Mega Pascha vs. Energy Density in Joule Per Millimeter. The Trend Line Slope ≈ 0, The Probability Value Is Significantly Greater Than 0.05.

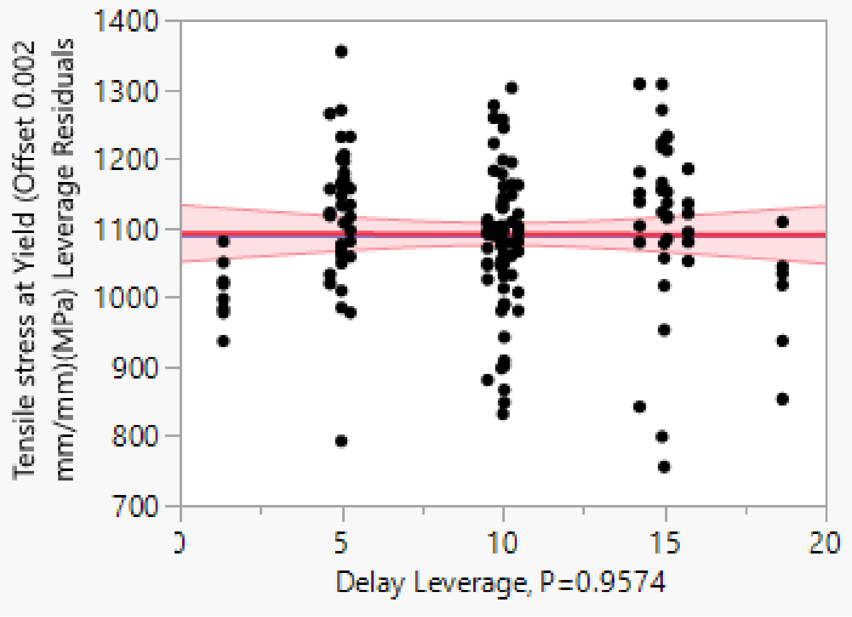

Figure 3.26 Yield Stress in Mega Pascha vs. Inter-layer Delay in Seconds. The Trend Line Slope ≈ 0, The Probability Value Is Significantly Greater Than 0.05.

The ultimate tensile strength shown in Figure 3.27 through 3.29 appear to be significantly affected by the parameters comparing with the yield stress. All three plots in terms of ultimate tensile strength individually versus laser power, energy density, and inter-layer delay are showing trend lines with slopes as the parameter levels change. The probability values are significantly less than 0.05, all the 3 hypotheses of laser power, energy density, or inter-layer delay individually referring to ultimate tensile strength are valid. The slopes of ultimate tensile strength versus laser power or energy density trend lines have less than 0 slopes. The ultimate tensile strength of the DOE samples decreases as the laser power or energy density increases. Oppositely, the slope of ultimate tensile strength versus inter-layer delay trend line has greater than 0 slope. The ultimate tensile strength of the DOE samples increases as the inter-layer delay increases.

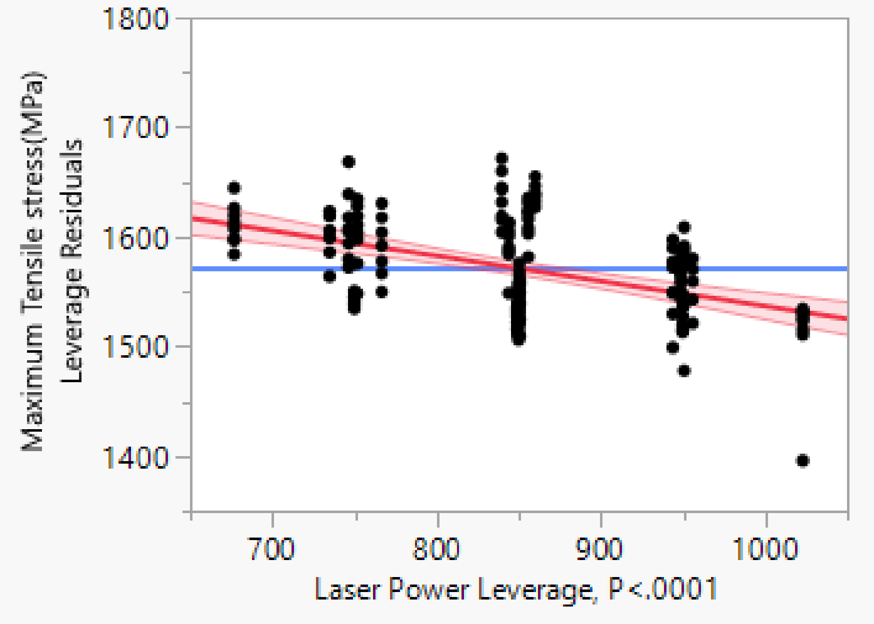

Figure 3.27 Ultimate Tensile Strength in Mega Pascha vs. Laser Power in Watt. The Trend Line Slope < 0 The Sample Ultimate Tensile Strength Decreases as The Laser Power Increases. The Probability Value Is Significantly Less Than 0.05.

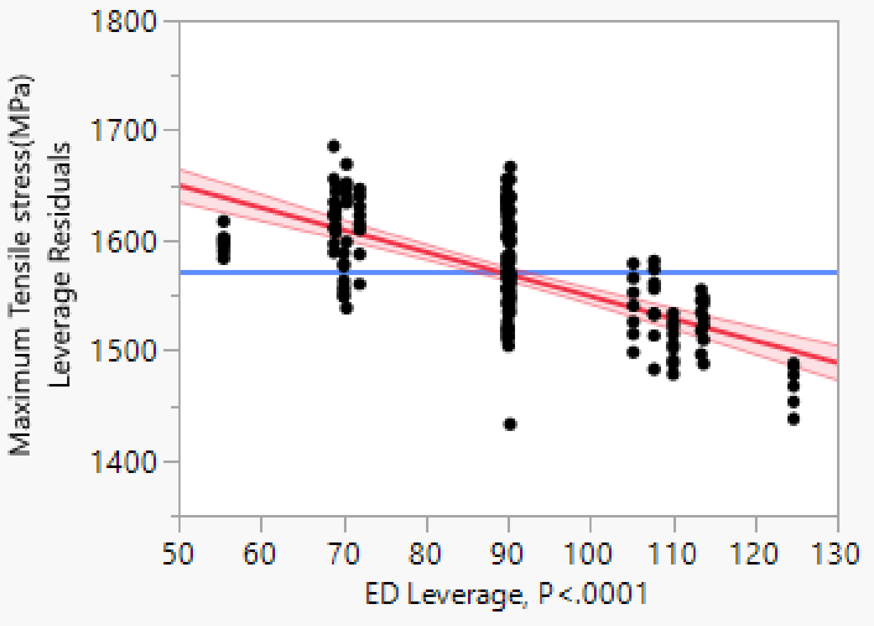

Figure 3.28 Ultimate Tensile Strength in Mega Pascha vs. Energy Density in Joule Per Millimeter. The Trend Line Slope < 0. The Sample Ultimate Tensile Strength Decreases as The Energy Density Increases. The Probability Value Is Significantly Less Than 0.05.

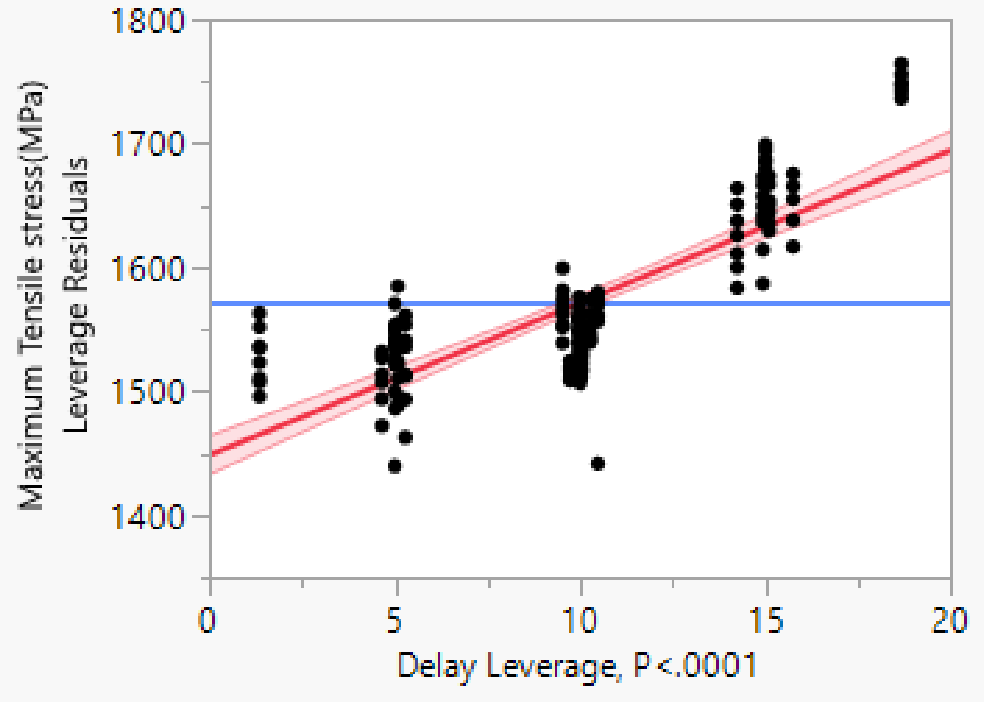

Figure 3.29 Ultimate Tensile Strength in Mega Pascha vs. Inter-layer Delay in Seconds. The Trend Line Slope > 0. The Sample Ultimate Tensile Strength Increases as The Inter-layer Delay Increases. The Probability Value Is Significantly Less Than 0.05.

The elongation shown in Figure 3.30 through 3.32 appear to be obviously more affected by the parameters than yield stress. All three plots in terms of elongation individually versus laser power, energy density, and inter-layer delay are showing trend lines with slopes as the parameter levels change. The probability values are significantly less than 0.05, all the 3 hypotheses of laser power, energy density, and inter-layer delay individually referring to elongation are valid. The slopes of elongation versus laser power or energy density trend lines have greater than 0 slopes. The elongation of the DOE samples increases as the laser power or energy density increases. Oppositely, the slope of the elongation versus inter-layer delay trend line has less than 0 slope. The elongation of the DOE samples decreases as the inter-layer delay increases.

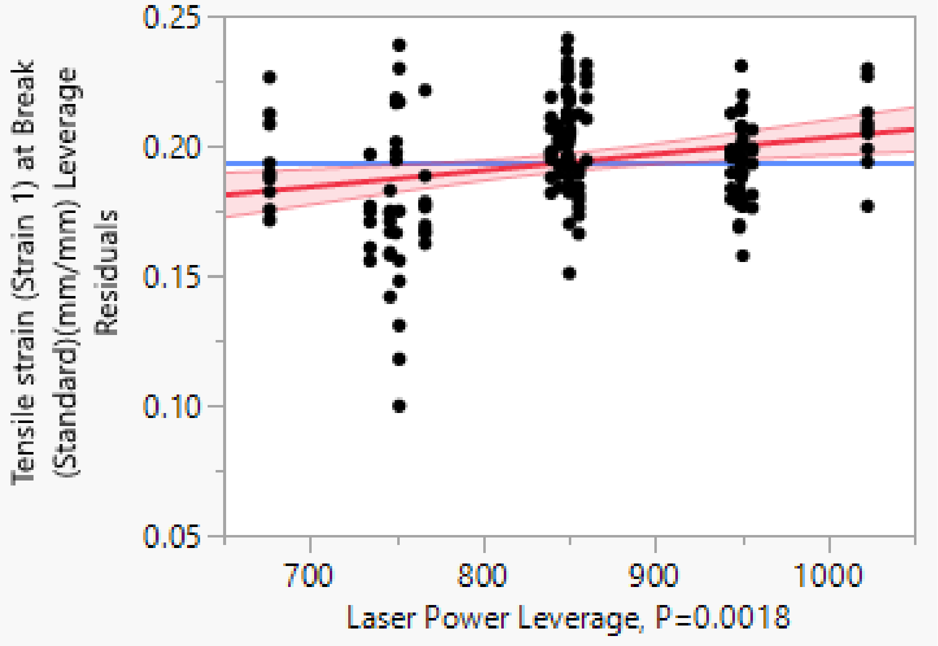

Figure 3.30 Elongation in Decimals vs. Laser Power in Watt. The Trend Line Slope > 0. The Samples’ Elongations Increase as The Laser Power Increases. The Probability Value is Significantly Less Than 0.05.

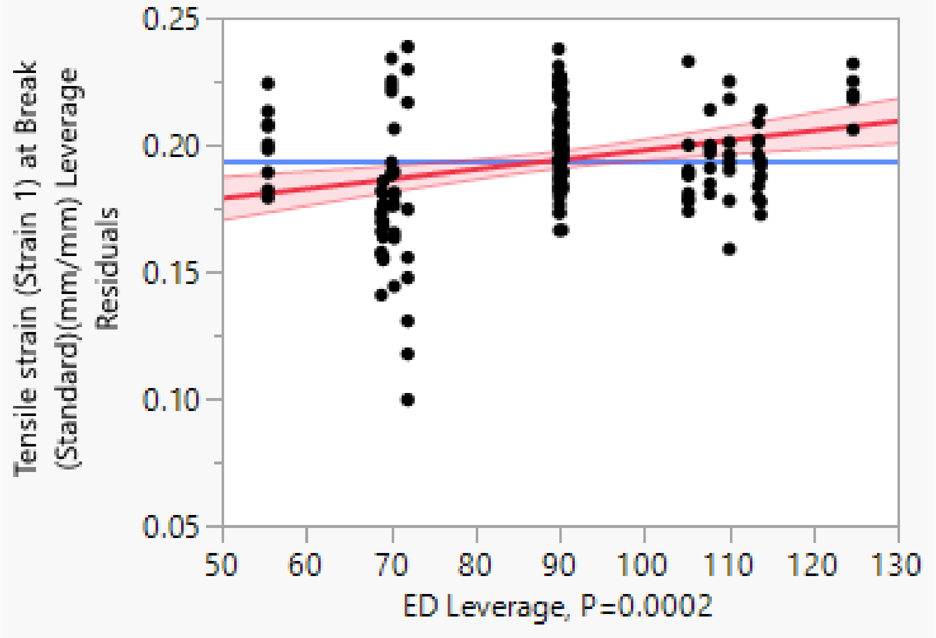

Figure 3.31 Elongation in Decimals vs. Energy Density in Joule Per Millimeter. The Trend Line Slope > 0. The Samples’ Elongations Increase as The Energy Density Increases. The Probability Value Is Significantly Less Than 0.05.

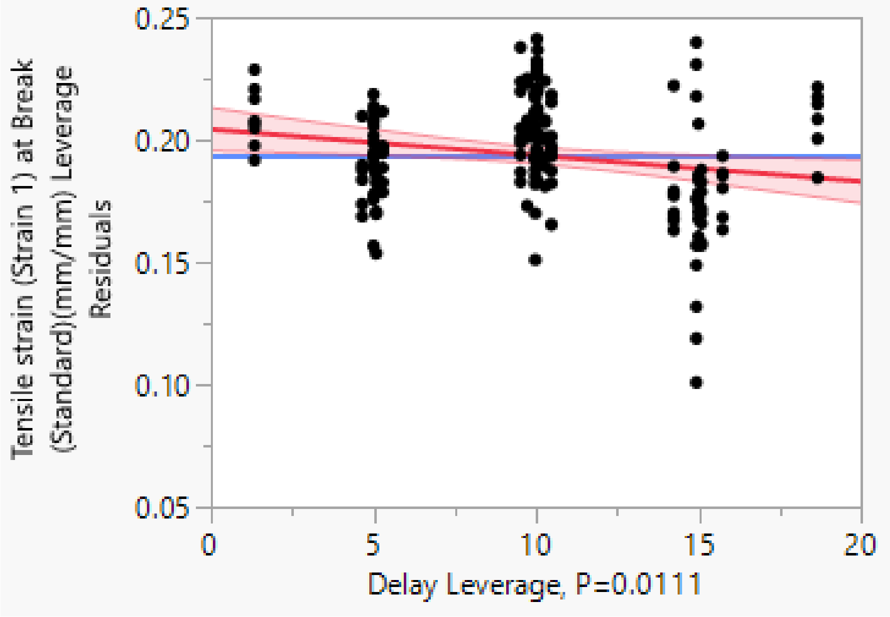

Figure 3.32 Elongation in Decimals vs. Inter-layer Delay in Seconds. The Trend Line Slope < 0. The Samples' Elongations Decrease as The Inter-layer Delay Increases. The Probability Value Is Significantly Less Than 0.05.

3.4.2.2. Interactive factors. Likewise, as shown in Figure 3.33 the single factor linear fit models, all the four probability values are greater than 0.05. The four interactive factors' fit models of laser power, energy density, and interlayer delay versus yield stress are flat which implies that the interaction parameters have minor effects to the tensile results. The flat trendline observed at either single factors or interaction factors agree with the nature of the material that the yield strength is more related to the composite of the material than the process parameters.

From the side view, the phenomenon implies that the uncontrolled factors at this point are drastically limited. The null hypothesis can be rejected as by varying the input factors the tensile results generally remain the same, and the tested tensile results are dominated by the selected parameters.

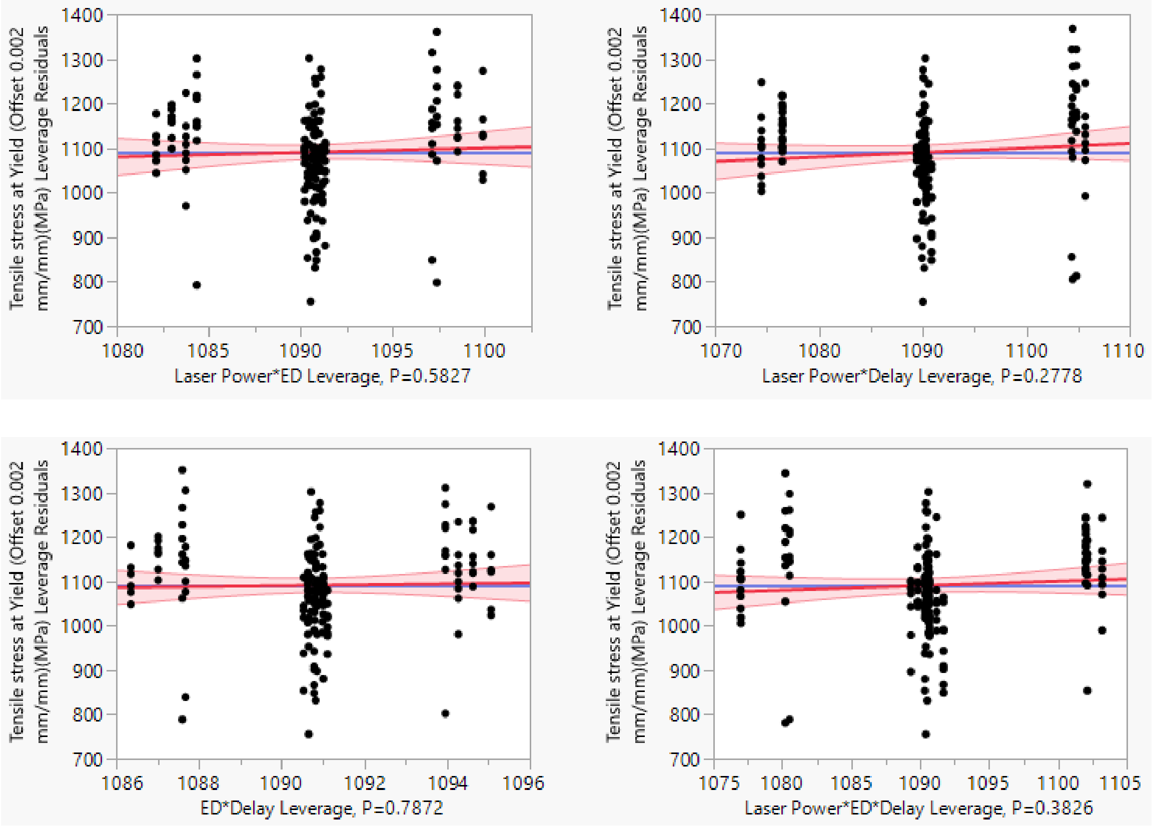

Figure 3.33 Fit Models of Interactive Factors vs. Yield Stress. All The Four Probability Values Are Greater Than 0.05. All The Four Linear Fit Models Are Flat.

As shown in Figure 3.34, the probability values of the two linear fit models of laser power cross energy density versus ultimate tensile strength and the energy density cross interlayer delay versus ultimate tensile strength are less than 0.05. The ultimate tensile strength values slightly increase as the two interactive factors of laser power cross energy density and energy density cross interlayer delay increase. The other two interactive factors of laser power cross interlayer delay and laser power cross energy density cross interlayer delay have greater than 0.05 probability values, their effects on ultimate tensile strength are negligible.

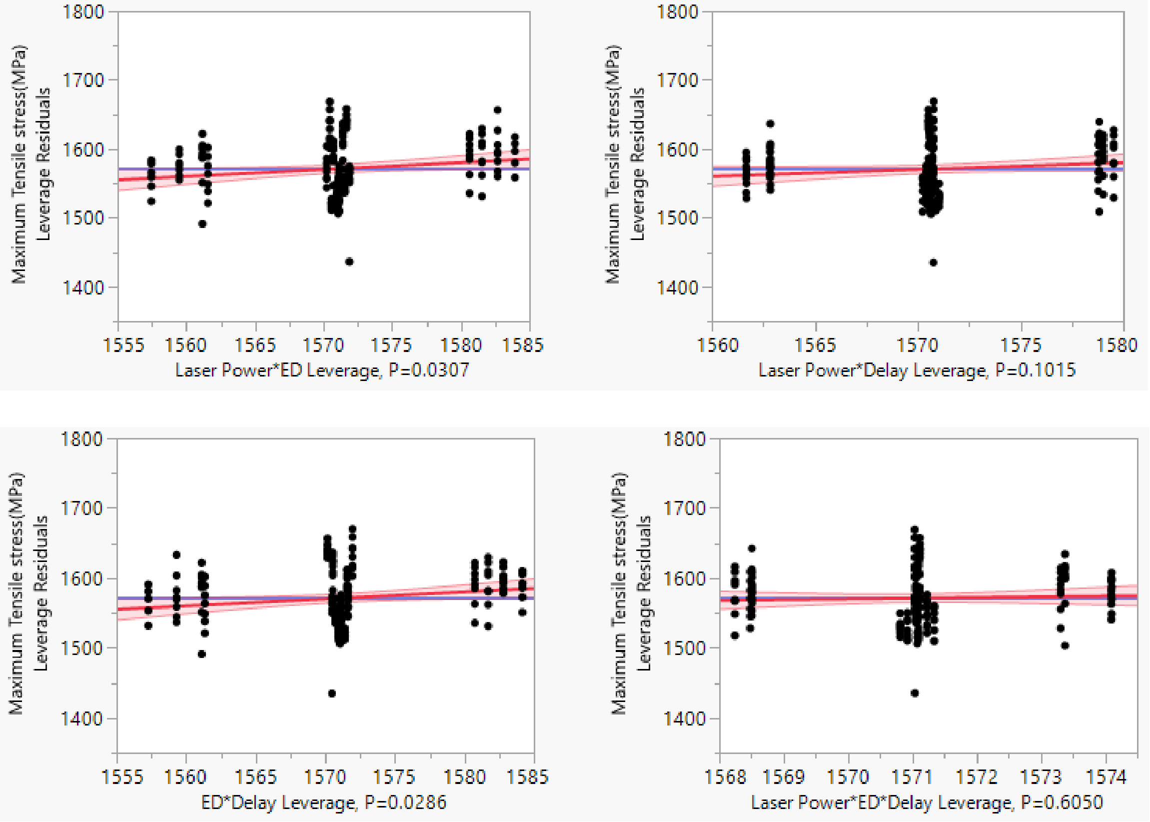

Figure 3.34 Fit Models of Interactive Factors vs. Ultimate Tensile Strength.

As shown in Figure 3.35, the two probability values of laser power cross energy density vs. elongation leverage and energy density cross interlayer delay vs. elongation leverages are less than 0.05 for slightly positive effect trends.

The two probability values of laser power cross interlayer delay vs. elongation leverage and laser power cross energy density cross interlayer delay vs. elongation leverages are greater than 0.05 for non-effect trends.

The probability values of the two linear fit models of laser power cross interlayer delay versus elongation and laser power cross energy density cross interlayer delay versus elongation are less than 0.05. Their elongation leverages slightly increase as the two interactive factors of laser power cross interlayer delay and laser power cross energy density cross interlayer delay increase. The fit models of laser power cross energy density versus elongation leverage and the energy density cross interlayer delay versus elongation leverages have greater than 0.05 probability values, their effects on elongation leverages are negligible.

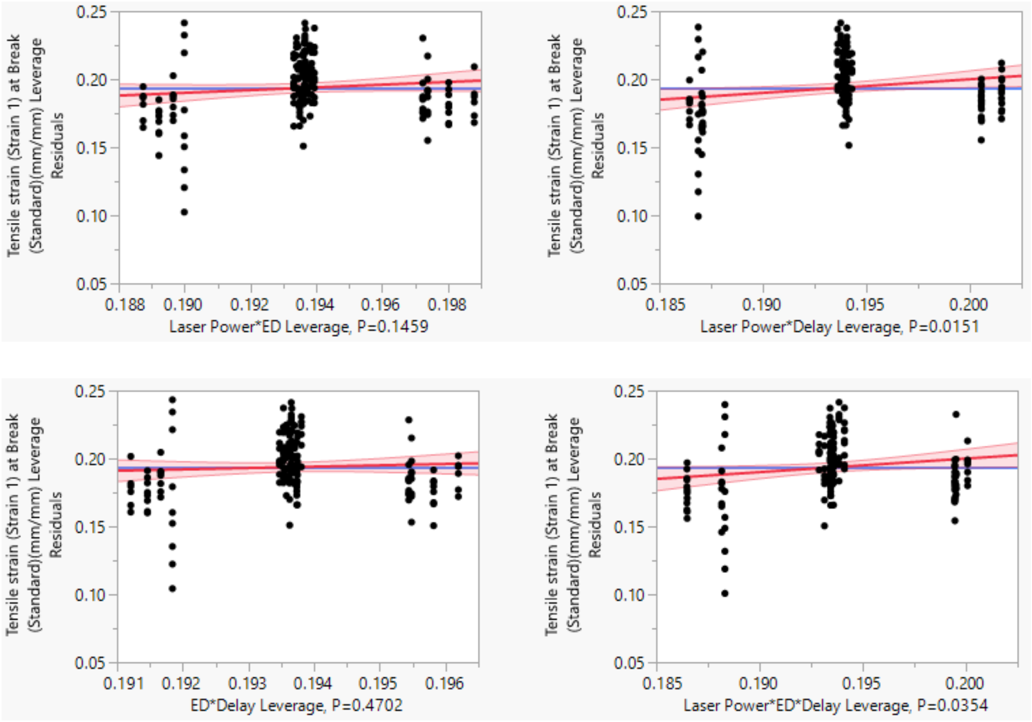

Figure 3.35 Fit Models of Interactive Factors vs. Elongation.

As shown in Figure 3.36, the two probability values of laser power cross interlayer delay vs. elongation leverage and laser power cross energy density cross interlayer delay vs. elongation leverages are less than 0.05 for slightly positive effect trends which implies that the interaction parameters have minor effects to the tensile results.

The two probability values of laser power cross energy density vs. elongation leverage and energy density cross interlayer delay vs. elongation leverages are greater than 0.05 for non-effect trends.

Based on the micro-tensile result from the 168 MT2 pieces. The probability values in effect summary shows all P values are less than 0.05. Delay has the greatest effect to the DOE micro-tensile results. The three single factors have zero P values, and their log worth values are 36 to 9 time greater than the crossed effects.

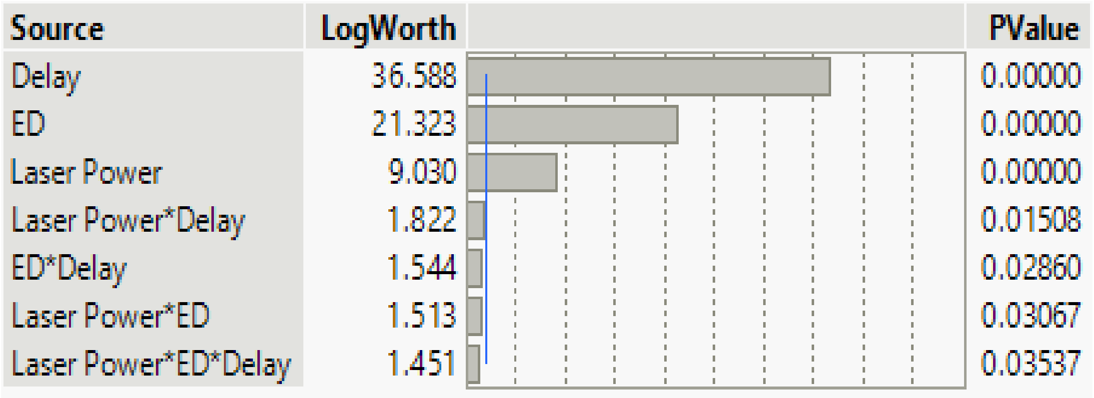

Source	LogWorth	PValue
Delay	36.588	0.00000
ED	21.323	0.00000
Laser Power	9.030	0.00000
Laser Power*Delay	1.822	0.01508
ED*Delay	1.544	0.02860
Laser Power*ED	1.513	0.03067
Laser Power*ED*Delay	1.451	0.03537

Figure 3.36 Effect Summary of Probability Values of the 168 Successfully Tested MT2 Specimens. All P Values are Less than 0.05. Delay Has the Greatest Effect to the DOE Micro-tensile Results. The Three Single Factors Have Zeros P Values Which Their Log Worth Values are 36 to 9 time Greater Than the Crossed Effects.

3.5. HARDNESS PROPERTIES

The DED processed samples during the stage 1 have been tested for Vickers hardness. The general hardness of AF9628 ranges from 400 HV to 500HV.

3.5.1. Stage 1 Present Hardness Data. The DED processed AF9628 hardness results are obtained from stages 1. The results range from 400HV to 500HVwhich is higher than most of the conventional steels.

Table 3.5 Sample 1 2 5 8 Local and Global Vickers-hardness Value Referring to Process Parameters and Test Parameters.

	Sample 1	Sample 2	Sample 5	Sample 8
Laser Power (W)	350	400	300	350
Scan Speed (mm/min)	200	200	250	250
Delay B/W Layers (s)	10		No Delay	
Press Force (N)	9.81			
Press Time (s)	10			
Magnification	40x			
Local Mean Hardness Value at Each Tested Location (HV)	437	439	488	488
	443	425	476	476
	425	448	492	492
	449	434	490	490
	440	431	490	490
	437	420	480	480
	443	428	474	474
	422	427	473	473
	434	434	490	490
	443	417	477	477
	442	423	458	471
	428	426	471	465
Global Mean Hardness (HV)	437	429	480	481
Global S.D.	8	8	10	9

3.5.2. **Discuss Parameters' Effect on Hardness.** All the 11 samples are tested at room temperature for Vickers-hardness, and all samples are tested for relatively high Vickers-hardness values. [7] [8] [9] [10] [11] The results of samples 1 2 5 and 8 are selected for comparison, their hardness results are shown in Table 3.5. Sample 1 and sample 2 are deposited with 10 seconds delay between each layer, and sample 5 and sample 8 are without delay between each layer. Based on the global mean hardness value, sample 1 is closer to sample 2 in hardness, both are around 430 HV. Sample 1 is tested 8 HV higher than sample 2. Both sample 5 and sample 8 tested about 480 HV, and both are 35 HV higher than sample 1 and sample 2.

The parameter differences of laser power and scan speed played a minor factor in the variance of sample Vickers-hardness. The factor leading to the major difference in Vickers-hardness results can be the different cooling rates. When the sample is deposited with 10 seconds delay, the sample cooled down more compared to a layer-by-layer process. The temperature is further decreased and more residual of stress is released compared with the samples deposited without delay between each layer. The cooling rate of the samples deposited without delay is more compared to the casting process, as the cooling time between each layer is shorter, the whole part cooled down as an entire body, hence more residual of stress is trapped and resulted in the sample in a higher Vickers-hardness.

4. CONCLUSION

The AF9628C low steel alloy tensile property is related to its hardness property. One relatively increases as the other relatively decreases. The cooling rate is a significant factor for AF9628C low steel alloy to weigh the properties. A process of 10 s delay between each layer resulted in higher values in UTS and elongation, as well as lower values in YS and hardness. A process of no delay between each layer resulted in higher values in YS and hardness, along with lower values in UTS and elongation.

4.1. MICROSTRUCTURE

Stage 1: The uniform surfaces are seen under SEM backscatter compo mode at both sample 1 and sample 2, which states no significant composition difference across the polished area along the sample build direction. On the other hand, the atomic mass distribution of sample 1 and sample 2 are uniform as the uniform brightness surfaces are seen under SEM BSE-COMPO mode. The difference found between sample 1 and sample 2 micro-structure is limited, the major difference of sample 1 and sample 2 is the defect density which resulted in the two samples with different micro-tensile results.

Stage 2: In the two data sites #8 and #5, sample #8 has the smaller grain size and variance of grain size however the sample #8 and #5 are both small comparing with other samples. Sample #8 and #5 have the same energy per length, but the Sample #8 has much longer delay time which yields higher cooling rate forming smaller grain sizes. In sample # 5 the interlayer delay time is much shorter which yields a smaller thermal gradient to retain more energy between layers forming larger grains comparing with sample #8.

The two elongation comparison samples have lower energy per length than the two UTS comparison samples. The max elongation sample has much shorter interlayer delay which more heat could be trapped to enable the grains grow more completely during the process. The repeating remelting between each layer could enable the grains of the max elongation sample keep growing along the vertical build direction.

4.2. TENSILE PROPERTIES

Stage 1: Both sample 1 and sample 2 with 10 seconds delay are tested over 20% elongation, whereas the samples processed with no delay are all tested less than 10% elongation. An over 1800 MPa mean UTS is tested at Sample 2. However, the YS of sample 1 and sample 2 are both tested about 100 to 150 MPa lower than other samples processed with no delay between each layer. As the longer delay between each layer, the more heat will be emitted and conducted, the alloy grain can be more evenly formed. As the alloy grains are formed evenly, the stress is more uniformly distributed on the sample body and less likely to accumulate over the break threshold at one point as the elongated distance increased, hence higher elongation percentage and UTS are tested at sample 2.

Stage 2: In the two data sites #8 and #5, sample #8 the smaller grain size the higher UTS, in the meantime both elongations are approximately the same as the grain size of the sample #8 and #5 are both small comparing with other samples. Sample #8 and #5 have the same energy per length, but the sample #8 has much smaller grain sizes which relates to its high UTS feedback. As the sample # 5 has larger grains due to lower cooling rate which yields larger grain size, its UTS results is tested lower comparing with sample #8.

Comparing with sample #15 and #13, the grain size of the max elongation is larger than the grain size of the min elongation. The sample #15 has smaller UTS comparing with sample #13. The UTS and elongation correspondingly have inverse relationship. The reason of sample #13 has the lowest elongation should be resulted in the micro-structural formation during the manufacturing process. Sample #13 has the second lowest energy per length and the second longest interlayer delay, insufficient heat could be retained so that grains are formed even less completely than the other samples. In addition, the diffusion problems and high numbers of dislocations are likely causing the brittle behavior of the sample. In the meantime, the Fe3C quantities is detected high, which could be also causing sample #13 to be brittle. The high variance of the sample #13 tensile result curves in elongation shown in Figure 3.17 can also proof sample #13 being brittle.

4.3. HARDNESS PROPERTIES

Stage 1: Sample 1 and sample 2 in stage 1 are tested relatively lower Vickers-hardness values than the samples processed with no delay between each layer. The difference in Vickers-hardness results can be sourced to the different cooling rate. The over low melt pool cooling rate during solid-state phase transformation transformed mostly Austenite into Pearlite and the over high cooling rate during solid state phase transformation transformed Austenite mostly into Martensite. Both the Pearlite and Martensite can result the sample in higher hardness results [16,17]. The melt pool temperature in both delay and no delay processes are relatively constant when melt pools are formed. The melt pools of the samples deposited with no delay solidified and transformed slower as the cooling time between each laser scan is shorter, less heat conducted, the temperature of the solidified part of the sample is higher, the melt pool solidified and transformed under low temperature deference between the melt pool and the early solidified part of the sample. In addition, the melt pools of the samples deposited with delay solidified and transformed faster as the cooling time between each laser scan is longer, more heat conducted, the temperature of the early solidified part of the sample is lower, the melt pool solidified and transformed under high temperature deference between the melt pool and the early solidified part of the sample.

The melt pool firstly solidified into Austenite. Bainite can only be transformed from Austenite within certain temperature region during the solid-state phase transformation. The temperature decreasing paths of each sample are nonlinear in both delay and no delay deposition processes. The cooling time in each temperature regions could be different from sample to sample and layer to layer during each heating and cooling cycle. The different dwell time at each temperature region resulted in different percentages of Austenite are transformed into Bainite phases during each solid-state phase transformation after the melt pool solidified into Austenite [18,19]. In this study, the factor of the samples with 10 seconds delay turned to be more durable than the samples processed with no delay can be that the time delay kept the Austenite temperature changing paths a longer time within the Bainite forming region, hence higher percentages of phase are transformed into Bainite during the solid-state phase transformation in those samples with 10 s delay. Above all, the AF9628 steel can be manufactured for tailored properties with the DED process by verifying the cooling method.

BIBLIOGRAPHY

[1] P. Agrawal et al., “Microstructure–Property Correlation in a Laser Powder Bed Fusion Processed High-Strength AF-9628 Steel,” Adv. Eng. Mater., vol. 23, no. 1, p. 2000845, Jan. 2021, doi: 10.1002/adem.202000845.

[2] E. M. Hager et al., “Development of high density parts in the low-alloy, high-performance steel AF9628 using laser powder bed fusion,” Materials Science and Engineering: A, vol. 838, p. 142656, Mar. 2022, doi: 10.1016/j.msea.2022.142656.

[3] R. Seede et al., “Effect of heat treatments on the microstructure and mechanical properties of an ultra-high strength martensitic steel fabricated via laser powder bed fusion additive manufacturing,” Additive Manufacturing, vol. 47, p. 102255, Nov. 2021, doi: 10.1016/j.addma.2021.102255.

[4] C. Tan et al., “Superior strength-ductility in laser aided additive manufactured high-strength steel by combination of intrinsic tempering and heat treatment,” Virtual and Physical Prototyping, vol. 16, no. 4, pp. 460–480, Jul. 2021, doi: 10.1080/17452759.2021.1964268.

[5] R. Seede et al., “An ultra-high strength martensitic steel fabricated using selective laser melting additive manufacturing: Densification, microstructure, and mechanical properties,” Acta Materialia, vol. 186, pp. 199–214, Mar. 2020, doi: 10.1016/j.actamat.2019.12.037.

[6] C. R. Hasbrouck, A. S. Hankey, R. Abrahams, and P. C. Lynch, “Sub-Surface Microstructural Evolution and Chip Formation During Turning of AF 9628 Steel,” Procedia Manufacturing, vol. 48, pp. 559–569, 2020, doi: 10.1016/j.promfg.2020.05.083.

[7] P. Chaitanya, R. Goud, R. Raghavan, M. Ramakrishna, K. G. Prashanth, and S. Gollapudi, “Technical Note: Hardness, Corrosion Behavior, and Microstructural Characteristics of a Selective Laser Melted 17-4 PH Steel,” Corrosion, vol. 78, no. 6, pp. 465–472, Jun. 2022, doi: 10.5006/3962.

[8] K. Wada, J. Yamabe, and H. Matsunaga, “Mechanism of hydrogen-induced hardening in pure nickel and in a copper–nickel alloy analyzed by micro Vickers hardness testing,” Materials Science and Engineering: A, vol. 805, p. 140580, Feb. 2021, doi: 10.1016/j.msea.2020.140580.

[9] C. F. Tan and M. R. Said, “Effect of Hardness Test on Precipitation Hardening Aluminium Alloy 6061-T6,” Chiang Mai J. Sci., p. 11.

[10] M. Z. Butt et al., “Nitrogen Ions Implantation in W-Based Quad Alloy: Structure, Electrical Resistivity, Surface Roughness and Vickers Hardness as a Function of Ion Dose,” Metals and Materials International, vol. 27, no. 9, pp. 3342–3358, Sep. 2021, doi: 10.1007/s12540-020-00861-z.

[11] S. C. Krishna, N. K. Gangwar, A. K. Jha, and B. Pant, “On the Prediction of Strength from Hardness for Copper Alloys,” Journal of Materials, vol. 2013, pp. 1–6, Apr. 2013, doi: 10.1155/2013/352578.

[12] M. Salandre, S. Garabedian, G. Gaillard, T. Williamson, and T. Joffre, “Development of a New Tooling Steel (L40) for Laser Powder Bed Fusion: Influence of Particle Size Distribution and Powder Atomization on Mechanical Performance,” Adv Eng Mater, vol. 23, no. 9, p. 2100350, Sep. 2021, doi: 10.1002/adem.202100350.

[13] "Grain boundary strengthening - Wikipedia", En.wikipedia.org, 2022. [Online]. Available: https://en.wikipedia.org/wiki/Grain_boundary_strengthening. [Accessed: 21- Jul- 2022].

[14] B. Zhang et al., “An efficient framework for printability assessment in Laser Powder Bed Fusion metal additive manufacturing,” Additive Manufacturing, vol. 46, p. 102018, Oct. 2021, doi: 10.1016/j.addma.2021.102018.

[15] J. Inoue, S. Nambu, Y. Ishimoto, and T. Koseki, “Fracture elongation of brittle/ductile multilayered steel composites with a strong interface,” Scripta Materialia, vol. 59, no. 10, pp. 1055–1058, Nov. 2008, doi: 10.1016/j.scriptamat.2008.07.020.

[16] "What is Bainite - Bainitic Steel - Definition | Material Properties", Material Properties, 2022. [Online]. Available: https://material-properties.org/what-is-bainite-bainitic-steel-definition/. [Accessed: 14- Jun- 2022].

[17] "Grain boundary strengthening - Wikipedia", En.wikipedia.org, 2022. [Online]. Available: https://en.wikipedia.org/wiki/Grain_boundary_strengthening. [Accessed: 14- Jun- 2022].

[18] “Properties and Selection: Irons, Steels, and High-Performance Alloys,” p. 2521.

[19] "Bainite | Metallurgy for Dummies", Metallurgyfordummies.com, 2022. [Online]. Available: https://www.metallurgyfordummies.com/bainite.html. [Accessed: 14-Jun- 2022].

[20] https://www.advancedpowders.com/industries/ded#:~:text=We%20offer%20 powder %20in%20the,our%20biomedical%20and%20aerospace%20customers. Benefit from AP&C's highly spherical powders, 2023

VITA

Mianqing Yang worked as a Graduate Research assistant (GRA) under Dr. Frank W. Liou, and Teaching assistant (GTA) in the Mechanical Engineering department at Missouri University of Science and Technology (Missouri S&T). He received his master’s degree in Manufacturing Engineering from Missouri S&T in July 2023. He received his bachelor’s degree in Physics Engineering from Missouri Southern State University in 2019.